Chapter 5

Characterization of Model Nanocatalysts by X-ray Absorption Spectroscopy

Qi Wang and Anatoly I. Frenkel
Stony Brook University, Stony Brook, NY, United States

Chapter Outline

5.1 INTRODUCTION

5.1.1 Nanocatalysts and Their Applications

Clusters with sizes ranging from subnanometer to a few nanometers in diameter attract broad interest from both the scientific and technological perspectives due to their nonbulk-like properties. These particles are widely used as components in novel electronic, magnetic, and optical devices and most commonly as heterogeneous catalysts. Nanocatalysts, compared with their bulk counterparts, demonstrate enhanced catalytic activity, selectivity, and stability. Understanding the mechanism of their work requires precise synthesis methods and high accuracy in structural characterization, both of which are among the major goals in studies of nanocatalysts. With rapid rise of new synthetic methods aimed at controlling the architecture of nanoclusters and the

Studies in Surface Science and Catalysis, Vol. 177. http://dx.doi.org/10.1016/B978-0-12-805090-3.00005-X

characterization methods that validate it, many fascinating details about their structural and electronic properties have emerged. For example, the continuous band structure of metal breaks up into discrete electronic states when particle size approaches the Fermi wavelength of an electron [1]. Correspondingly, for large clusters, the optical absorption spectra show one optical absorption peak assigned to the surface plasmon resonance. The absorption frequency and line width are inversely proportional to the particle radius ($1/R$) [1]. For small clusters, there are multiple absorption peaks assigned to single-electron intraband resonances; thus, some clusters (e.g., Cu, Ag, and Au) exhibit strong fluorescence emission upon UV photoexcitation. The unique optical property makes those clusters good candidates for biolabels and light-emitting sources [2–4]. Analogously, simple scaling laws used to describe properties (such as ionization energy, electron affinity, melting temperature, and cohesive or binding energy) of large (>5–10 nm in size) clusters are no longer valid in the limit of ultrasmall (subnanometer to a few nanometer in size) clusters [1,5]. Other important characteristics derived from the finite size effects are multitudes of geometric forms (some well-known examples of nonbulk-like geometries are decahedron, cuboctahedron, and icosahedron) [6] and compositions (clusters can feature core/shell, cluster by cluster, or other more exotic motifs). All these parameters have significant influences on cluster properties. For instance, the surface geometry affects thermal properties [7], strain [8,9], position of the d-band center [10], and stability of valence shell [11], all of which are regarded to be descriptors of their catalytic activity.

The increasing demands for studying functional nanomaterials under realistic working conditions add challenges to their investigation due to the fact that the cluster properties can be affected by the surroundings, such as ligands, organic solvents, supports, and gases. These environmental parameters are often sensitive to and thus can change in the result of operating conditions. Such sensitivity brings opportunities for making materials with novel properties [3,12,13], and, simultaneously, poses challenges for both experimental and theoretical methods in linking the properties of clusters to their size, shape, geometry, structure, and/or composition. This chapter summarizes latest advancements in experimental characterization of three-dimensional structures of metal clusters in the size range of subnanometer to a few nanometer by extended X-ray absorption fine structure (EXAFS) spectroscopy.

5.1.2 Solving the Structure in Model Nanocatalysts

Herein, we will briefly review the experimental methods that are among the most commonly used for characterization of the size, shape, geometry, and atomic structure of clusters. We also address the challenges the small size and nonbulk-like behaviors of clusters and their sensitivity to environments pose to some of the characterization approaches. Scanning tunneling

microscopy, atomic-force microscopy, (scanning) transmission electron microscopy ((S)TEM), and X-ray photoelectron spectroscopy (XPS) are widely utilized techniques for cluster characterization. Electron microscopy (EM) methods are most commonly employed for the purpose of imaging and observing cluster size/shape/structure and their transformations, due to their high resolving capability [6]. The latter diminishes significantly during in situ/operando measurements (e.g., growth of nanoparticles [14,15] and structure evolution in realistic catalytic environments [16]). One exception is the environmental TEM/STEM, which can be used for in situ/operando studies with atomic resolution in gaseous or liquid atmospheres at pressures up to a fraction of 1 atm [17–21]. The rest of the methods listed above has been used predominantly for elucidating the electronic structure (e.g., binding energy) [22] and revealing elemental composition of clusters [23] that can also be measured by combining STEM and electron energy loss spectroscopy [24]. Though the availability of high-flux X-rays produced by synchrotron radiation enables XPS measurements at ambient pressure (AP-XPS) for gases environments [23] and for liquid/solid interfaces [25], it is still challenging to take high-quality data under realistic growing/working conditions, because of the surface sensitivity of the XPS. Bragg X-ray diffraction (XRD) and small-angle X-ray scattering (SAXS) can also provide information about particle size and are routinely used in operando conditions. However, Bragg XRD requires long-range order of atomic arrangements. SAXS reveals low resolution (1–2 nm) structures, and the extracted size/shape information strongly relies on the analysis method [26].

Because of its inherent complexity, the characterization of supported metal catalysts relies on the use of multiple complementary techniques to provide a complete picture. A good approach with considerable promise to improve characterization is the combination of experiment and theory into a correlated, multitechnique analysis scheme, as summarized by Billinge and Levin [27]. Multitechnique characterization is a powerful method for better understanding catalytic reaction mechanisms, but its predictions will remain limited if the correlated experiments are not performed in the same conditions [28–31]. The need to investigate clusters in harsh environments of catalytic reactions, that is, under high temperature and/or pressure, further complicates their analysis. In particular, it has been demonstrated in several studies that results obtained under operation conditions can differ quite significantly from those acquired in static, pre- or postreaction measurements [32–34]. The most frequently used in situ or operando methodologies are based on scattering or spectroscopy techniques, including XRD [35–37], XAS (XANES and EXAFS)[36,37], XPS [38], Auger spectroscopy [39], Mössbauer spectroscopy [40], magnetic resonance (ESR and NMR) [41,42], UV/VIS spectroscopy [43,44], vibrational spectroscopy (IR and Raman) [44,45], and thermal desorption spectroscopy [46]. Another challenge to the quantitative accuracy of these methods is the ensemble averaging nature of the spectra. Such

averaging may provide only incomplete or even incorrect information in terms of the underlying structural properties and reaction dynamics, especially when the particle size, shape, and/or compositional distributions are broad and/or asymmetrical.

In this chapter, we will focus on model nanoparticles, those possessing well-defined sizes and shapes. We will make a particular emphasis on EXAFS for their characterization because (1) it is a particularly widely used in situ technique, (2) it can be easily applied in various kinds of environments, (3) it exhibits high temporal resolution (e.g., Quick EXAFS or QEXAFS [47]), and (4) the EXAFS method provides comprehensive knowledge about structural and electronic properties at the local scale, without the need to have ordered structures and/or bulk dimensions [48–51].

5.2 CHARACTERIZATION OF MODEL NANOCATALYSTS BY EXAFS

5.2.1 EXAFS Application in Nanomaterials Research

X-ray absorption fine structure (XAFS) spectroscopy is a premier technique for measuring both electronic and atomic local structures around different atomic species in materials. XAFS can be divided into two parts: X-ray absorption near-edge structure (XANES) and EXAFS. XAFS has advantages over many other techniques by being feasible to many different sample types, including solutions, powders, pellets, and films. It can easily adapt to in situ/operando modes (e.g., time-, temperature-, pressure-, electric/magnetic field-, and gas-dependent), a vital capability for studying functional materials of the future and new modes of applications [28,52]. Compared with the EM-based techniques that probe a few hundreds to thousands of particles, XAFS provides excellent statistical information due to the large fluxes (10^{10}–10^{14} photons per second interrogating the sample) available at today's synchrotrons. Different from the X-ray scattering methods, most of which are restricted to the materials with long-range order, XAFS detects local structure that makes it ideal for investigation of small (less than 10 nm in diameter) clusters where large disorder is expected. Additionally, due to its elemental specificity, XAFS is capable of studying heterometallic nanocatalysts.

In XAFS, fine structure in the resonance region of the X-ray absorption coefficient (called the absorption edge) is measured in either transmission or fluorescence detection mode. The XANES region (within 30 eV below to 40 eV above the edge) contains information about the electronic structure and local geometry of the absorbing atom and its nearest neighbors. The post-edge region that extends from ~40 eV to between 1000 and 1500 eV (depending on the system) past the edge contains an oscillatory signal and is known as EXAFS [53]. The origin of the fine structure in EXAFS is the interference

between the incoming and scattered photoelectron waves. The interference pattern contains quantitative information about the local atomic environment in the proximity of the absorbing atom. The frequency of these oscillations can be quantitatively related to the distances between the absorbing atom and atoms within a given coordination shell around it. The EXAFS signal therefore contains information about interatomic distances and their disorders (due to the static and dynamic displacements of all atoms from their average positions). The amplitude of these oscillations correlates with the number of neighboring atoms of a given type and their phase—with the identity of the scattering atomic species—thus providing chemical sensitivity to the EXAFS method. Because EXAFS originates from the absorbing of X-ray photons by selected (by X-ray energy) atomic species and not all atoms in the sample, this technique has elemental specificity: all structural information is defined with respect to a specific atomic species (which exhibit resonant absorption of X-rays in the given energy range). In that respect, EXAFS is different from, for example, pair distribution function (PDF) method of total X-ray scattering, which obtains the environmental radial distribution function (RDF) in the sample, not partial RDF as in EXAFS.

The oscillatory part of the absorption coefficient— $\chi(k)$ —contains the sum of all contributions $\chi_i(k)$ from groups of neighbor atoms at approximately equal distances from the absorbing atoms (i.e., within the ith shell), which are often written as [54]

$$\chi_i(k) = \frac{S_0^2 n_i}{kR_i^2} \left| f_i^{\text{eff}}(k) \right| \sin\left[2kR_i - \frac{4}{3}\sigma_i^{(3)} k^3 + \delta_i(k) \right] e^{-2\sigma_i^2 k^2} e^{-2R_i/\lambda_i(k)}, \qquad (5.1)$$

where k is the photoelectron wave number; $f_i^{\text{eff}}(k)$ and $\delta_i(k)$ are the photoelectron scattering-path amplitude and phase, respectively; S_0^2 is the passive electron reduction factor; n_i is the degeneracy of the scattering path; R_i is the effective half-path length (which equals the interatomic distance for single scattering paths); σ_i^2 is the mean-square deviation in R_i; $\sigma_i^{(3)}$ is the third cumulant of the RDF [55]; and $\lambda_i(k)$ is the photoelectron mean free path. The most dominant contribution to the EXAFS signal originates from backscattering of the photoelectron by neighboring atoms toward the absorbing atom (single scattering). More complex scattering patterns involve the electron wave's reflections by multiple atoms [56]. This multiple scattering approach is essential in order to accurately calculate the absorption coefficient. For example, the contribution from multiple scattering by atoms along an atomic row, known as the shadowing or focusing effect, can dominate the backscattering. The amplitude reduction factor S_0^2 describes the intrinsic losses upon excitation, which arise due to the many-body effects during the photoabsorption process. The scattering amplitudes and phases, along with the photoelectron mean free paths for different scattering configurations contributing to the EXAFS signal, are calculated ab initio. Among the most widely used software

programs for these calculations are FEFF (versions 6 [54], 8 [57], and 9 [58]), EXCURVE [59], and GNXAS [60].

Due to the relatively large penetration depth of hard X-rays (tens of micrometers), many reactors are available for in situ and operando studies in gases and liquids, electrochemical or fuel cell studies, and even ones for high-pressure and high-temperature conditions [37,61–69]. High brilliance third-generation synchrotron sources further enable the investigation of low concentrations of catalysts and the use of submicron X-ray beams for spatially resolved XANES and EXAFS measurements. Another important characteristic of synchrotron X-ray absorption spectroscopy (XAS) experiments is the extremely short (10^{-15}–10^{-16} s) lifetime involved in X-ray absorption. For this reason, XANES and EXAFS are found in many studies and applications that require high temporal resolution [70].

For an in-depth description of the different aspects of EXAFS methodology, the reader is referred to other resources [56,71–75]. Detailed discussion of specialized methods suitable for the characterization of nanoparticle size, shape, and atomic structure, based on multiple scattering analysis of EXAFS data, has also been recently reported [66,76–80]. Also of interest are several recent reviews outlining XAS-based applications to structural and catalytic studies of nanomaterials [81–84]. In the following sections, we will review some of these recent developments.

5.2.2 Methods of Analysis of Monometallic Nanocatalysts

5.2.2.1 Size, Shape, Morphology of Well-Defined Clusters

Fourier-transformed (FT) EXAFS spectra of metal clusters, similar to other systems probed by EXAFS, exhibit one or more peaks corresponding to the contributions of different photoelectron paths that connect the absorbing atom and its neighboring atoms. These paths can be analytically expressed in terms of the three structure-related parameters that are unique for each path and can be quantified by fitting the theoretical EXAFS spectrum to the experimental data. They are coordination number (CN), bond distance (R), and the mean-square bond-length disorder, also known as EXAFS Debye-Waller factor (σ^2). Among them, CN is a key parameter used for determination of the size and shape of well-defined clusters. For homometallic atomic pairs, the CN is defined as the average number, per absorber of type A, of nearest neighbors of the same type A within a given coordination shell:

$$n_i = \frac{2N_{\mathrm{AA}(i)}}{N_{\mathrm{A}}}. \tag{5.2}$$

Here, n_i is the coordination number of the ith shell at the radius R_i around the absorbing atom in a monometallic cluster, $N_{\mathrm{AA}(i)}$ is the total number of

the A-A nearest neighbors within the same coordination shell, and N_A is the total number of A-type atoms in the cluster. The factor of two in Eq. (5.2) is due to the fact that each atom of the A-A pair is an absorber, and thus, the number of these pairs should be doubled in calculating the A-A coordination numbers.

For small monometallic clusters, EXAFS spectra usually show one prominent peak in *r*-space, located between 2 and 3 Å. This peak can be, depending on the type of absorbing atom, split into two or more peaks due to the Ramsauer-Townsend resonance [85–87], corresponding to the first nearest-neighbor (1NN) metal-metal pair interaction. Using the coordination number of this pair measured in EXAFS analysis, several methods are available for estimating the size of nanoparticles. One such method was proposed by Montejano-Carrizales et al. [88,89]. They obtained that the geometric characteristics of regular polyhedra can be analytically expressed as a function of one parameter, the cluster order (L), defined as the number of spacings between adjacent atoms along the edge of the cluster [88]. This method can be expanded to many morphologies and cluster families [90]. For example, the truncated cuboctahedral model with the (111) plane parallel to the support is most close to the morphology found in many supported metal clusters (Fig. 5.1). The relationship between N_1 and L in a truncated cuboctahedron is [91]

$$N_1 = \frac{3(20L^3 + 21L^2 + 7L)}{5L^3 + 12L^2 + 10L + 3}. \tag{5.3}$$

For truncated cuboctahedron with atom numbers of 10 ($L=1$), 37 ($L=2$), 92 ($L=3$), and 185 ($L=4$), the first nearest coordination numbers are 4.8, 7.0, 8.2, and 8.9, respectively.

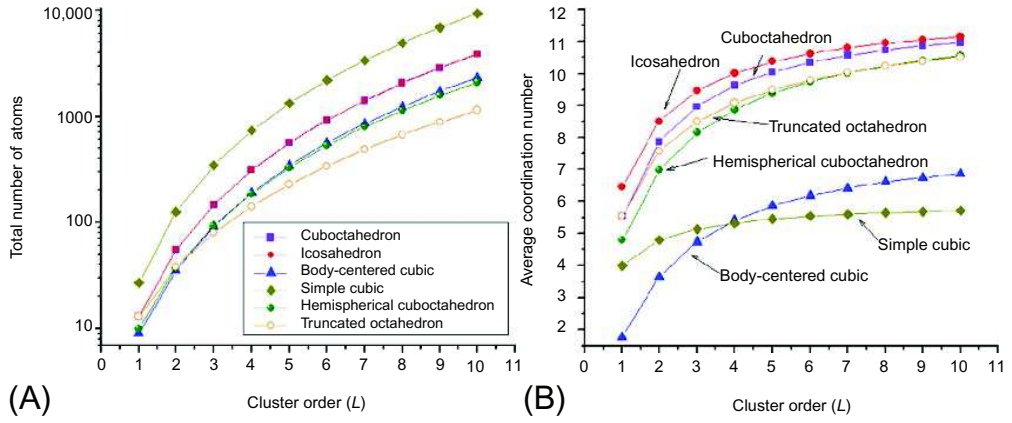

FIG. 5.1 Cluster order L ($0 \le L \le 10$)-dependent changes of total number of atoms (A) and average coordination number (B) for cuboctahedron, icosahedron, body-centered cube, simple cube, hemispheric cuboctahedron, and truncated octahedron.

Calvin et al. developed another useful method to estimate the size of quasispherical clusters [92]. In this method, the average coordination number n_i of the ith shell is written as

$$n_i = \left[1 - \frac{3}{4}\left(\frac{r_i}{R}\right) + \frac{1}{16}\left(\frac{r_i}{R}\right)^3\right] N_i. \tag{5.4}$$

In Eq. (5.4), N_i is the ith shell coordination number of the corresponding bulk counterpart of the nanocluster, r_i is the scattering path length for the ith shell, and R is the radius of cluster. Although Eq. (5.4) results in inaccurate values of the coordination numbers for small clusters, this method provides good estimates for coordination numbers for larger clusters. The advantage of this approach is that the cluster radius can be directly extracted from the fit by using Eq. (5.4). Another advantage of the latter method over the first one is that it takes into account single scattering paths at larger distances. Indeed, the size/geometry of clusters, no matter how narrow is the cluster size distribution, cannot be obtained only with the knowledge of the first nearest coordination number. The reason for that is the correlation between the cluster size and shape in terms of their effects on the 1NN coordination numbers. For instance, as shown in Fig. 5.1, the average coordination numbers of the 55-atom icosahedron and 79-atom truncated octahedron are both close to 8.5; hence, the knowledge of the 1NN CN is not sufficient to refine the cluster size, shape, and structure. For studying ideal polyhedral clusters, Frenkel et al. proposed to use multiple scattering contributions for refining the cluster size, structure, and shape self-consistently, by utilizing different functional behaviors of the 1NN, 2NN, 3NN, 4NN, and 5NN coordination numbers as a function of the cluster size [66,78,77].

Another challenge in calculating coordination numbers is the irregular geometries of relaxed clusters, such as those generated by first principle calculations. In such case, analytic calculations cannot be performed. Frenkel et al. proposed to use a histogram-based method, where a RDF of the nearest neighboring shells is calculated for any given set of atomic coordinates, and the coordination numbers are then obtained by integrating the RDF within the shells of interest [90,93]. Using the previously described example of the challenge in separating the 55-atom icosahedron from the 79-atom truncated octahedron, the degeneracy of the 1NN CNs will be lifted when comparing n_2 or even n_3 due to their uniqueness for each of these two geometries (icosahedron, $n_2 = 2.18$ and $n_3 = 8.73$ and truncated octahedron, $n_2 = 3.19$ and $n_3 = 11.54$). As emphasized, another advantage of this method is that it is not limited by the shapes and symmetries of a very small number of regular polyhedral clusters, making it a very robust strategy for size/geometry determination.

We will briefly demonstrate how the histogram method [90,93] works. This approach employs computer-generated cluster coordinates. The cluster-average pair radial distribution function $\rho(r)$ is computed for a cluster of N atoms:

$$\rho(r) = \frac{1}{N}\sum_{i=1}^{n}\rho_i(r), \quad \rho_i(r) = \frac{dN_i}{dR_i}, \tag{5.5}$$

where $\rho_i(r)$ is the partial RDF for an atom i and dN_i is the number of its neighbors within the spherical shell of thickness dR_i. The subsequent calculation of coordination numbers for an arbitrary coordination shell (between R_1 and R_2) is achieved by integrating the $\rho(r)$:

$$n_i = \int_{R_1}^{R_2}\rho(r)dr. \tag{5.6}$$

Compared with the two methods described above, the RDF method enables rapid calculation of coordination numbers of clusters with arbitrary sizes and shapes. By combining EM with multiple scattering EXAFS analysis and data modeling, several geometries with the same sequence of coordination numbers of the nearest-neighbor shells can be discriminated [78,94].

As mentioned above, when the analysis of EXAFS data extends beyond the 1NN contribution, multiple scattering effects should be included in the model. To illustrate this point, Fig. 5.2 includes the fourth nearest-neighbor single scattering (SS4), collinear focusing triple scattering (TS), and collinear focusing double scattering (DS) paths in a face-centered cubic (*fcc*) lattice. By using multiple scattering analysis, Frenkel et al. were able to identify the icosahedral geometry of monolayer protected Au_{13} cluster [95,96] and determine the shapes of well-defined supported nanoclusters [78,77,94].

As another example of the multiple scattering EXAFS analysis of the cluster shape, we use the structural modeling of carbon-supported Pt NPs up to the fourth/fifth Pt-Pt shell [78,77]. Fig. 5.3 illustrates such analysis for size and shape determination and shows that the (111)-truncated hemispheric cuboctahedron provides a good approximation for the 10 wt% Pt/C sample, with a particles size of about 1.7 nm [78]. To find connections between particle shape and catalytic properties, γ-Al_2O_3-supported Pt NPs with various shapes

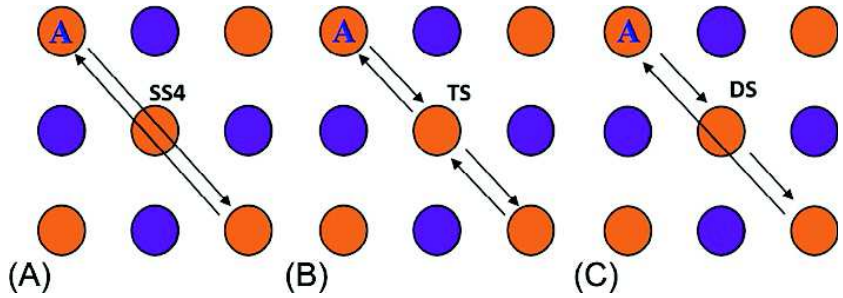

FIG. 5.2 Schematic representation of (A) fourth nearest-neighbor single scattering (SS4), (B) collinear focusing triple scattering (TS), and (C) collinear focusing double scattering (DS) paths in a face-centered cubic lattice. In each figure, the absorbing atom is labeled with "A," *orange atoms* (light gray in print versions) are in plane, and *purple atoms* (dark gray in print versions) are located above the plane.

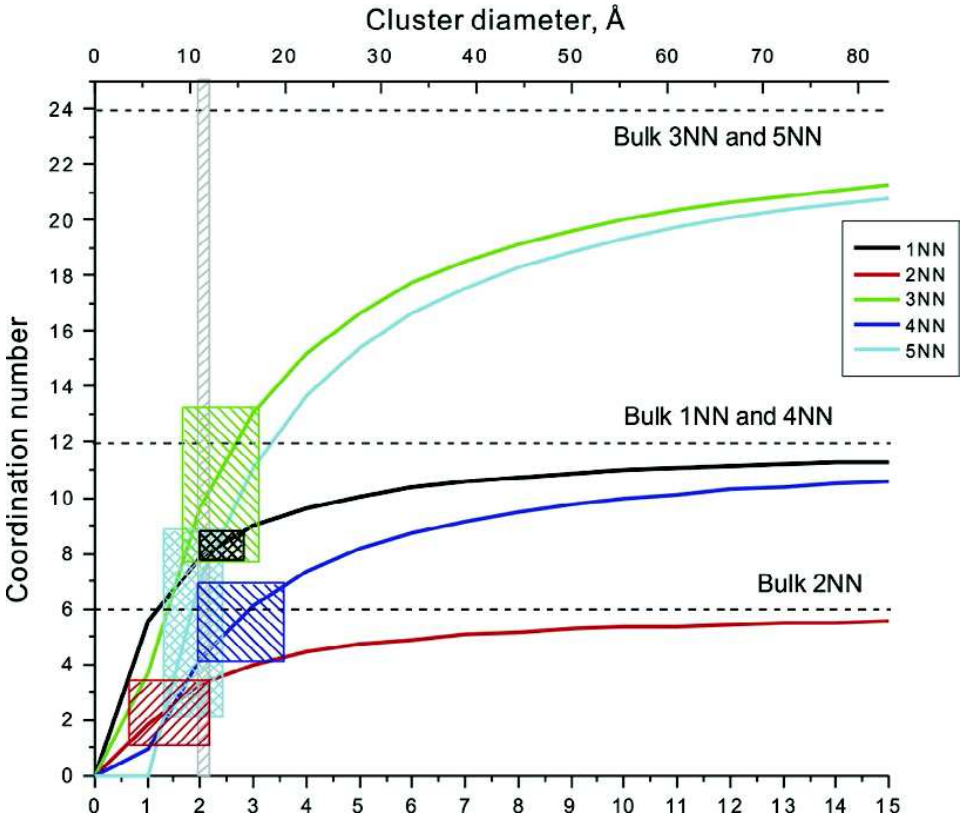

FIG. 5.3 Comparison of the average distances (up to 5NN), together with their error bars (shown as *shaded rectangles*), measured by EXAFS for the 10 wt% Pt/C sample and the calculated from a truncated (by (111) plane) cuboctahedron for cluster orders L up to 15. *(Reproduced with permission from A.I. Frenkel, C.W. Hills, R.G. Nuzzo, A view from the inside: complexity in the atomic scale ordering of supported metal nanoparticles, J. Phys. Chem. B 105 (51) (2001) 12700. Copyright 2001 American Chemical Society.)*

but analogous average size (~1 nm) were prepared and characterized by multiple scattering analysis (up to fourth shell) of EXAFS data, in combination with microscopic tools [97]. The shape having higher percentage of undercoordinated atoms (at the edge or corner sites) on the surface was found effective for lowering the onset temperature for 2-propanol oxidation [98].

Jentys also proposed to estimate the mean size and shape of clusters by comparing a set of coordination numbers obtained by EXAFS analysis with those of models with different geometries [99]. This method uses a hyperbolic function to correlate the relationship between the average coordination number of the ith ($1 \leq i \leq 5$) shell and the total atom number in a *fcc* cluster:

$$n_i = \frac{aN_A}{b+N_A} + \frac{cN_A}{d+N_A}. \tag{5.7}$$

With the known information on 13–7500-atom clusters, the parameters (a, b, c, and d) were quantified by applying a nonlinear least square fitting.

The particle shape was found to have minor influence to the coordination numbers of the first and second nearest shells but significant influence to those of the higher shells. Therefore, two steps were suggested for size/shape determination. First, cluster size can be estimated using n_1. Second, one can further determine cluster shape by comparing the ratio of n_3 with n_1. A similar idea was extended by Beale and Weckhuysen to a larger number of atom packings and shapes with the use of the Hill function [100].

5.2.2.2 Adsorbate and Support Effects on Metal-Metal Bond Strains

Due to the ensemble-averaging nature of EXAFS, determination of surface-specific strain by EXAFS is complicated, but several strategies have been assessed recently to isolate the surface contribution to strain from that of the bulk. For example, Erickson et al. obtained a change in the Pt-Pt bond length in the nanoparticles in response to the exposure to either O_2 or N_2 gas [101]. In this work, Pt-Pt bond lengths measured in the 1 nm in diameter nanoparticles immobilized in the electrochemical cell were shown to change, depending on the gas flown into the cell (Fig. 5.4A and B). While the distribution of strain within the bonding framework is impossible to extract from this average method, its upper and lower bounds can be estimated by assuming two extreme models. The "bulk strain" model corresponds to the uniform bond expansion, where all bonds change by the experimentally observed amount ΔR (Fig. 5.4B). The second model describes the experimentally observed expansion as the superposition of the two subsets of bonds: the surface ones, expanded, and the rest, unchanged. Using a 35-atom cluster (Fig. 5.4C) as a simplified model, Ericksen et al. obtained quantitative estimates of the surface-localized strain. The second model allowed generating the surface-localized bond expansion, ΔR (Fig. 5.4D), and the surface-localized strain via

$$\varepsilon = \frac{\Delta R}{R}, \tag{5.8}$$

and the stress in the cantilever film via Stoney's equation. The agreement between the calculated stress-thickness values from EXAFS and from in situ cantilever measurements was excellent, thus validating the model used. This example highlights a direct link between the microscopic strains in nanoparticles measured at the subpicometer scales and their macroscopic implications (here—on the cantilever measurements).

In addition to strain measurements, EXAFS analysis allows to evaluate energetic characteristics associated with local deformations of interatomic bonds. In elastic approximation, local strain energy averaged over the ensemble of bonds can be calculated by EXAFS, as it was done, for example, in Ref. [102] and, later, modified in Ref. [8]:

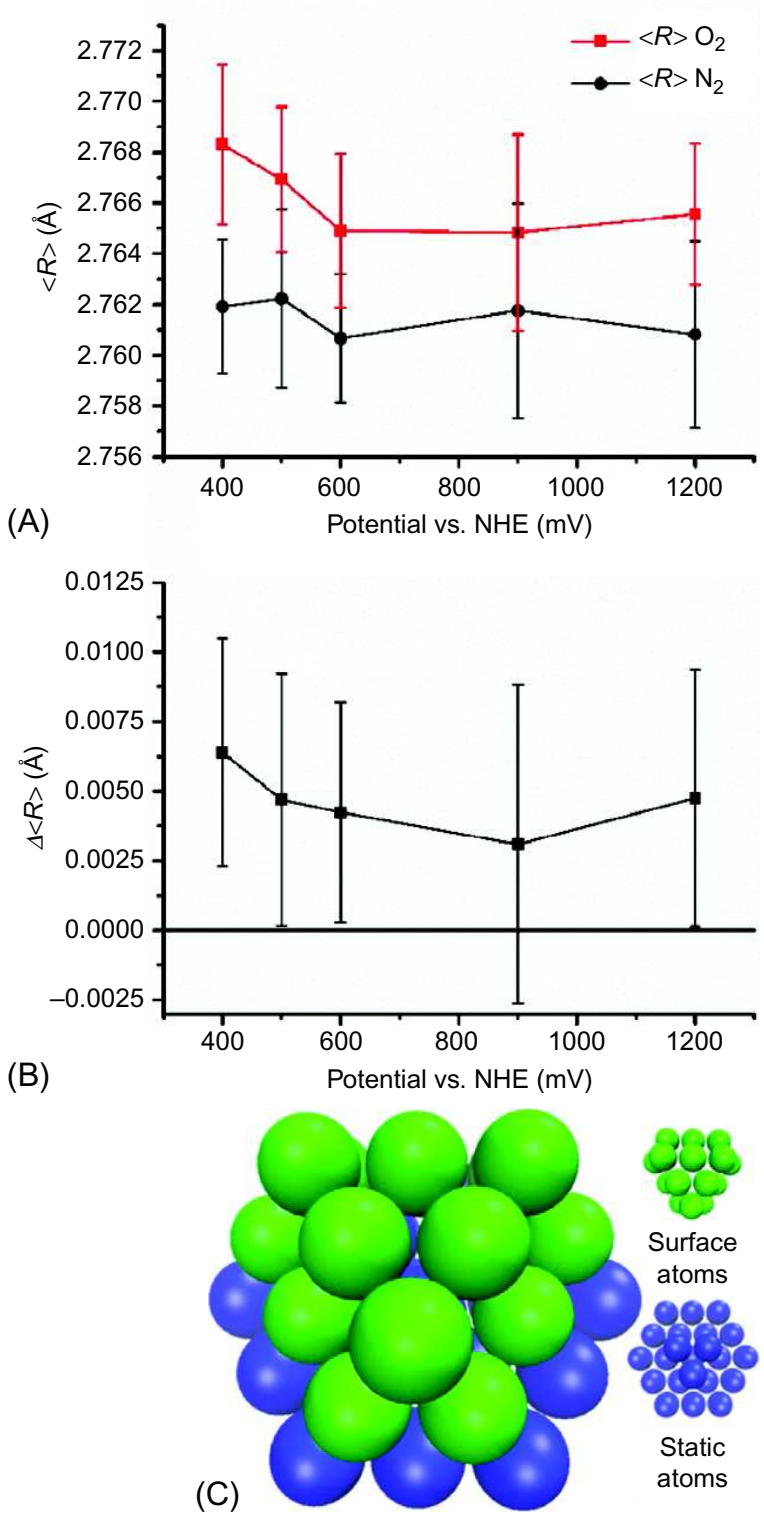

FIG. 5.4 (A) Pt-Pt bond distances under N_2 and O_2 at different potentials; (B) ΔR at all potentials, showing bond expansion upon exposure to O_2; (C) depiction of the 37 nanoparticles, showing static atoms (blue; dark gray in print versions) and dynamic surface atoms (green; light gray in print versions); and (D) minimum and maximum Pt-Pt surface bond expansion under O_2 calculated from the ensemble measurement and surface-restricted expansion. *(Reproduced with permission from E.M. Erickson, M.E. Oruc, D.J. Wetzel, M.W. Cason, T.T.H. Hoang, M.W. Small, et al., A comparison of atomistic and continuum approaches to the study of bonding dynamics in electrocatalysis: microcantilever stress and in situ EXAFS observations of platinum bond expansion due to oxygen adsorption during the oxygen reduction reaction. Anal Chem. 86 (16) (2014) 8372–8373. Copyright 2014 American Chemical Society.)*

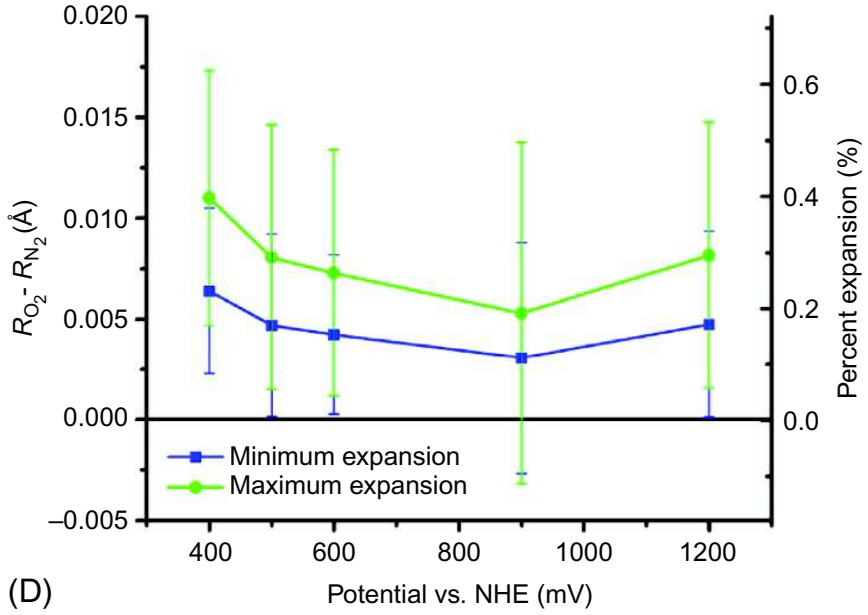

FIG. 5.4—Cont'd

$$U = \frac{1}{2} N k \sigma^2. \tag{5.9}$$

Here, U is the total elastic energy per atom, N is the metal-metal (M-M) coordination number, k is the force constant of the M-M bond, and σ^2 is the EXAFS Debye-Waller factor. In the harmonic approximation, the force constant is $k = \mu\omega^2$, where $\mu = m/2$ is the reduced mass of the M-M bond, $\omega = k_B \Theta_E / \hbar$ is the Einstein frequency, $\hbar$ is Planck's constant, and Θ_E is the Einstein temperature. When static (temperature-independent) strain is present, Eq. (5.9) can be written as the sum of two contributions: $U = V(T) + W$, where $V(T)$ arises due to dynamic vibrations and W originates from the static disorder present in the system of interatomic bonds. These two terms can be separately evaluated by expressing σ^2 in terms of the dynamic and static terms (σ_d^2 and σ_s^2, respectively) of the EXAFS Debye-Waller factor:

$$\sigma^2 = \sigma_d^2 + \sigma_s^2. \tag{5.10}$$

The residual elastic strain energy due to the static disorder can then be calculated as Eq. (5.8)

$$U_s = \frac{1}{2} N k \sigma_s^2. \tag{5.11}$$

In harmonic approximation, the force constant k can be found from the Einstein temperature measurement within the same EXAFS experiment. Eq. (5.11) can be used in for a wide range of materials, from bulk to nanoscale, as long as the coordination numbers of particular species and their

dynamic characteristics are known. As shown many times in EXAFS analysis, the local distortions from the average structure, obtained at the length scale of just a few interatomic distances around atomic species may be important for explaining materials properties at much larger length scales. For example, in Ref. [102], it was demonstrated that the residual strain energy due to the bond-length mismatch in bulk binary alloys maximized in the middle of the concentration range and was sufficiently large to explain the melting point suppression of the alloys. X-ray powder diffraction measurements confirmed the existence of microstrain in binary alloys and provided independent estimate of the energy associated with the microstrain, showing that it is the important factor in thermal instability of the disordered phase of Au-Cu alloys at low temperatures [103,104]. In Ref. [8], it was shown that the strain energy of nanometer-scale metal catalysts is of the same order of magnitude with the chemisorption energy of adsorbates, and, hence, should be taken into account in fundamental theories of reactivity of nanocatalysts.

XAFS methods do not only possess the required accuracy to detect finite size effects in nanomaterials but can also illuminate the nature of the complex interactions of the components and their environment. One illustration of this is seen in a recent study of a Pt catalyst supported on both high surface area γ-Al_2O_3 and carbon substrates that revealed several aspects of anomalous behavior [105,106]. For example, γ-Al_2O_3-supported Pt particles of 1 nm average diameter demonstrated the following attributes: (1) an unexpected negative thermal expansion, revealed in the bond-length contraction at elevated temperatures; (2) size-dependent changes in the static disorder, revealed by the large *y*-intercept values linearly interpolated for the mean-square displacement of Pt-Pt distances; and (3) shifting of the onset of the Pt L_3 absorption edge to lower energies with increasing temperature. These findings demonstrate that the effects of substrate and adsorbates on the thermodynamic properties of metal nanoparticles are as important as the particle size, which has long been believed to be a dominant factor responsible for nonbulk-like properties (e.g., decrease of lattice parameters of small clusters compared with the bulk [107–109] or size-dependent changes in vibrational dynamics [109–113]). These results [106] show that the effects of the size, support, and atmosphere on the structural, dynamic, and electronic properties are of the same order of magnitude and are thus comparable. This highlights the need for new experimental and theoretical methodologies that are able to capture the details of substrate and adsorbate influences on the thermodynamic properties of the metal clusters in addition to details of cluster size, structure, and shape. An important requirement for such methods is that they are suited to measure all of these attributes for catalytic processes in situ while controlling pressure and temperature.

A recent illustration of this approach is the work by Small et al. [8], where the effect of gas concentration, pressure, and temperature on adsorbate coverage, structure, shape, and electronic state of Pt clusters supported on γ-Al_2O_3

was measured. The data in this study show that these effects can be modeled as arising from separable components. For example, coordination numbers and bond-length disorder were found to strongly correlate with adsorbate coverage and temperature. The γ-Al_2O_3-supported particles exhibited enhanced static disorder (and thus strain) at increased partial pressure (and thus coverage) of CO. An opposite trend was seen in an H_2 atmosphere. Furthermore, the metal-metal coordination numbers increased at high temperature under CO (at all partial pressures), indicating adsorbate-induced restructuring [114]. By independently varying the partial pressure of the gas and the system's temperature, this study revealed how the complex structural and electronic properties of this important—and representative—heterogeneous catalyst evolve under varying conditions. Specifically, it is found that CO elicits strong structural and electronic changes of the Pt nanoparticles, while H_2 adsorption mainly acts to relieve significant metal-metal bond strains. The XANES data indicated a series of contributions that were ascribed to particle-adsorbate, particle-support, and adsorbate-support interactions. The intertwining of these different contributions could be related to the patterns of condition-dependent charge exchange, which in turn mediates the catalysts' atomic and electronic structure:

$$S(T,P) = \frac{A}{\alpha(P)e^{-n/T}+1} + BT + C(P). \tag{5.12}$$

The first term in the right-hand side of Eq. (5.12) describes the metal-adsorbate interactions via the (P,T)-dependent adsorbate coverage, the second term the contribution of the metal-support interaction, and the last term, the adsorbate-support interaction. These data also show that charge exchange due to metal-support interactions is a dominant factor in the electronic structure changes observed for the working catalyst.

5.2.3 Methods of Analysis of Bimetallic Nanoparticles

5.2.3.1 Determination of Composition Patterns of Bimetallic Clusters

Heterometallic clusters composed of two or more metals are of great interest in a broad range of fields from electrocatalysis [24,115,116] to catalysis [23], information storage [117,118], biological labeling [119], and nanophotonics [120]. Among the factors affecting their properties, the most important ones are the size, morphology, and mixing patterns of different elements in the cluster. Several analytic methods developed on the basis of EXAFS data for characterizing heterometallic nanoclusters will be described here.

In nanoclusters, like in bulk alloys, one should discriminate between homogeneity and randomness. Both characteristics can be carefully characterized by EXAFS [121,84]. For example, different types of bimetallic configurations (homogeneous and heterogeneous with short-range order and

random) are demonstrated in Fig. 5.5. Compared with the cluster in Fig. 5.5A, which has perfect short (and long)-range order, the atomic distribution is random for the cluster in Fig. 5.5B. For such random alloys (A and B are mixed statistically), n_{AA} and n_{AB} are in the same ratios as the bulk concentrations of A and B atoms in the cluster:

$$\frac{n_{AA}}{n_{AB}} = \frac{x_A}{x_B}. \tag{5.13}$$

In Eq. (5.13), analogously to the definition of the coordination number for a homometallic pair (Eq. 5.2), the coordination number for heterometallic bonds is defined as

$$n_{AB} = \frac{N_{AB}}{N_A}. \tag{5.14}$$

It is also important to compare the average CN of the A-metal (AM) pairs, n_{AM}, with that of the BM pairs, n_{BM}. These indices are defined as $n_{AM} = n_{AA} + n_{AB}$ and $n_{BM} = n_{BA} + n_{BB}$. By analyzing EXAFS data, the quantitative information on n_{AA}, n_{AB}, n_{BA}, n_{BB}, n_{AM}, and n_{BM} can be obtained, and information about the patterns of mixing or segregation of alloying elements can be analyzed by modeling. As an illustration of the above, we will demonstrate how the values of n_{AM} and n_{BM} can be used to characterize the homogeneity of heterometallic clusters. For example, if $n_{AM} < n_{BM}$ and if the cluster size—and composition—distributions are narrow, this inequality points to the preferential location of A atoms near the surface, with smaller numbers of nearest neighbors, while B is preferentially located in the cluster core, where the coordination number of nearest neighbors is larger.

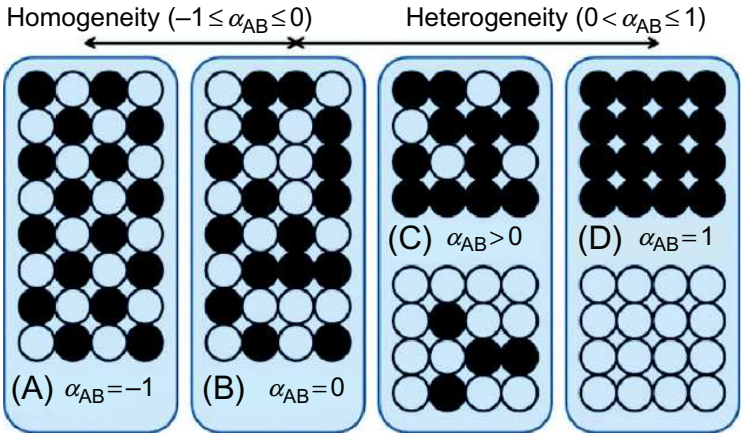

FIG. 5.5 Demonstration of homogeneous (A,B) and heterogeneous (C,D) packing of atoms with 50–50 composition. Each configuration can be characterized by a unique value of the short-range order parameter α. *(Reproduced with permission from A.I. Frenkel, Q. Wang, S.I. Sanchez, M.W. Small, R.G. Nuzzo, Short range order in bimetallic nanoalloys: an extended X-ray absorption fine structure study, J. Chem. Phys. 138 (6) (2013) 064202. Copyright 2013, AIP Publishing LLC.)*

For more formal characterization of segregation or mixing tendencies, including the characterization of randomness of well-mixed alloys, the short-range order parameter, α [121,84], similar to its definition by Cowley for bulk alloys [122–124], can be used:

$$\alpha = 1 - \frac{n_{AB}/n_{AM}}{x_B}. \tag{5.15}$$

As shown in Fig. 5.5, α can be applied to clusters with different degrees of homogeneity and randomness. The value varies in the interval between -1 and 1. For alloys that favor (disfavor) clustering of like atoms, α will be positive (negative). In two dimensions, it equals -1 for systems with perfect order, 0 for random alloys, and 1 for systems without the formation of heterometallic bond. This parameter is therefore essential for characterization of nanoalloys, such as core-shell, random, or cluster-on-cluster types.

In addition to the composition pattern, the cluster size can be determined by methods similar to those described above for monometallic particles with the knowledge of the average number of metal-metal neighbors per metal atoms:

$$n_{MM} = x_A n_{AM} + x_B n_{BM}. \tag{5.16}$$

The coordination numbers of homo- and heterometallic bonds can be extracted from XAFS data analysis, which should be done concurrently for both absorption edges with obvious constrains imposed on the heterometallic bonds:

$$n_{AB} = \frac{x_B}{x_A} n_{BA}, \quad R_{AB} = R_{BA}, \quad \sigma^2_{AB} = \sigma^2_{BA}. \tag{5.17}$$

To analyze higher-shell data, it is required to add the multiple scattering path contributions, which may be comparable with the amplitudes of the single scattering paths. Nashner and Frenkel et al. revealed the local metal coordination environment by multiple scattering analysis of the EXAFS data, which shows the segregation and migration of Pt from the core to the surface of $PtRu_5$ when temperature was changed under reducing atmosphere [66,76].

5.2.3.2 Solving Structures of Bimetallic Clusters With Overlapping Absorption Edges

Some bimetallic systems contain atomic species that are close to each other in the periodic table, for example, Ir and Pt or Pt and Au. The implication of that proximity for their XAFS data is that the extended high-energy region of the lower energy (e.g., Ir or Pt) edge spectrum leaks into the spectrum of the higher energy (Pt or Au, respectively) edge. This phenomenon is not limited to the heterometallic clusters but hampers analysis of any materials with adjacent absorption edges, for instance, Ti K-edge (4966 eV) and Ba L_3-edge

(5247 eV) of perovskite $BaTiO_3$. With overlapped XAFS spectra, their EXAFS analysis becomes problematic [125–127]. Menard et al. deconvoluted the EXAFS spectra of both edges by parameterizing the EXAFS signals of the lower and higher energy ranges in terms of the photoelectrons originating from their respective absorption edges [128]. For demonstration, Ir and Pt L_3-edge data were used, but this method could be extended to any arbitrary bimetallic composition. The overlapped EXAFS signals are split into three parts: (1) the Ir EXAFS until the Pt L_3-edge rise, (2) the Ir EXAFS contributing to the Pt L_3-edge EXAFS, and (3) the Pt EXAFS from the Pt L_3-edge. For the analysis of nearest-neighbor scattering paths, those three contributions could be described by the EXAFS equations:

$$\chi_{\text{Ir edge}}(k_{\text{Ir}}) = \frac{S_{0,\text{Ir}}^2 N_{\text{Ir}}}{k_{\text{Ir}} R_{\text{Ir}}^2} \left| f_{\text{Ir}}^{\text{eff}}(k_{\text{Ir}}) \right| \sin\left[2k_{\text{Ir}} R_{\text{Ir}} - \frac{4}{3}\sigma_{\text{Ir}}^{(3)} k_{\text{Ir}}^3 + \delta_{\text{Ir}}(k_{\text{Ir}}) \right] e^{-2\sigma_{\text{Ir}}^2 k_{\text{Ir}}^2} e^{-\frac{2R_{\text{Ir}}}{\lambda_{\text{Ir}}(k_{\text{Ir}})}}, \tag{5.18}$$

and

$$\begin{aligned} \chi_{\text{Pt edge}}(k_{\text{Pt}}, k_{\text{Ir}}) = {} & \frac{S_{0,\text{Pt}}^2 N_{\text{Pt}}}{k_{\text{Pt}} R_{\text{Pt}}^2} \left| f_{\text{Pt}}^{\text{eff}}(k_{\text{Pt}}) \right| \sin\left[2k_{\text{Pt}} R_{\text{Pt}} - \frac{4}{3}\sigma_{\text{Pt}}^{(3)} k_{\text{Pt}}^3 + \delta_{\text{Pt}}(k_{\text{Pt}}) \right] \\ & \times e^{-2\sigma_{\text{Pt}}^2 k_{\text{Pt}}^2} e^{-\frac{2R_{\text{Pt}}}{\lambda_{\text{Pt}}(k_{\text{Pt}})}} + \frac{A S_{0,\text{Ir}}^2 N_{\text{Ir}}}{k_{\text{Ir}} R_{\text{Ir}}^2} \left| f_{\text{Ir}}^{\text{eff}}(k_{\text{Ir}}) \right| \\ & \times \sin\left[2k_{\text{Ir}} R_{\text{Ir}} - \frac{4}{3}\sigma_{\text{Ir}}^{(3)} k_{\text{Ir}}^3 + \delta_{\text{Ir}}(k_{\text{Ir}}) \right] \times e^{-2\sigma_{\text{Ir}}^2 k_{\text{Ir}}^2} e^{-\frac{2R_{\text{Ir}}}{\lambda_{\text{Ir}}(k_{\text{Ir}})}}. \end{aligned} \tag{5.19}$$

The nonlinear least squares fitting of experimental data to Eqs. (5.18), (5.19) should be done concurrently. Further structural constraints are applied in the analysis: (1) The factor $A = \Delta\mu_{0,\text{Ir}}/\Delta\mu_{0,\text{Pt}}$, where $\Delta\mu_{0,\text{Ir}}$ and $\Delta\mu_{0,\text{Pt}}$ are the changes in the absorption at the edge steps, is included to account for differences in normalization of the two terms in the second part of Eq. (5.19); (2) the correction to the threshold energy (in eV) for the Ir EXAFS in the Pt L_3-edge is defined as $\Delta E_{0,\text{Ir}} - (349 + \Delta E_{0,\text{Pt}})$, where 349 eV is the difference between the tabulated threshold energies. Such a large energy shift is necessary in this method since it accounts for a unique $k = 0$ reference point for the Ir EXAFS extending beyond the Pt-edge when the Pt-edge EXAFS is transformed to k-space. Finally, Ir-M (or Pt-M) paths are used to describe both Ir-Ir and Ir-Pt (or Pt-Pt and Pt-Ir), since the backscattering amplitudes and phases of Ir and Pt as nearest neighbors to the absorbing atoms (Ir or Pt) are similar.

5.2.4 Limitations of EXAFS Methods for Analysis of Nanoclusters

We discussed how to determine the atomic structures of mono- and bimetallic nanoclusters by modeling EXAFS analysis results in Sections 5.2.2 and 5.2.3. Those examples clearly show the importance of coordination numbers of the

first neighbors of absorbing atoms. To monometallic nanoclusters, they can be used to determine particle size, shape, and morphology, while to bimetallic nanoclusters, they are also essential for determining the compositional patterns of samples. Those interpretations are made assuming the narrow size, shape, and composition distributions of nanoclusters. If such assumption is not justified and the clusters are, instead, broadly distributed over multiple forms of order, that assumption would result in the incorrect interpretation of the system. The artifacts that arise due to the broad range of sizes and compositions of cluster ensembles and corresponding corrective strategies that should be undertaken are described below.

Heterogeneity of bond length and compositional distributions is a common situation that not only happens in each individual cluster (intracluster heterogeneity) but also can be present due to the changes between multiple clusters (intercluster heterogeneity). As an example, catalytic particles undergo reduction and oxidation at different stages of the reaction, and their structure is thus strongly sensitive to the gradients of temperature and concentration (of reactants, intermediates, and products, as well as the catalytic species) that are unavoidable in real catalytic reactors and processes. If the sample consists of a heterogeneous mixture of reduced and unreduced species, the best-fit results of the coordination numbers are affected not only by the size and/or geometry of clusters but also by the volume fraction of the reduced clusters within the sample [79]. In the study by Sun et al., Pd cluster size revealed by EXAFS analysis was found much smaller than that measured by TEM due to the coexistence of disordered Pd-S compounds and metallic cluster cores [129]. From the ratio of the coordination numbers measured from EXAFS and calculated from the size obtained by EM, assuming a specific shape of clusters, the unknown volume fraction of nanoclusters could then be obtained [129]. Liu et al. recently investigated the structural dynamics of working nanocatalysts via combined XAFS and STEM. The average cluster size obtained from EXAFS analysis was also smaller than that from STEM measurements, indicating the existence of multiple sample species during catalytic reactions [115].

For small clusters, additional limitations of EXAFS analysis are related to the imperfections of the atomic order due to the effects of capping ligands [130], steric effects [131], crystalline defects [132], and interaction with adsorbates [133]. The enhanced surface tension, typical in nanoparticles, causes a decrease in the lattice parameter [107]. The bonds near the surface of nanoclusters are more strained than the ones inside the core, which accordingly results in a strong variation of the interatomic distances: the bond distance decreases from the interior of the cluster toward the surface [134,135]. Such a non-Gaussian form of interparticle disorder would cause a problem in EXAFS analysis if it is not properly accounted for in structure models. Yevick and Frenkel [136] examined the effects of surface disorder on the EXAFS modeling of metallic clusters by using two sample clusters

with 147 and 923 atoms, which are 1.7 and 3.4 nm in diameters, respectively. They employed the empirical distortion function $f(r)$ to each atom within the clusters to simulate surface tension effects:

$$f(r) = A + (1-A)\exp(Cr), \quad \text{where} = \frac{1}{R}\ln\left(\frac{B-A}{1-A}\right). \tag{5.20}$$

This distortion function satisfies the conditions $f(0) = 1$ and $f(R) = B \leq 1$ for the atoms at the center and the periphery, respectively. Multiplying the radial distortion function (Eq. 5.20) to all atomic coordinates yields the new positions of atoms in the distorted cluster. The parameter A, corresponding to the curvature of the distortion curve, can be changed in the range between 1.05 and 1.00001, to simulate uniformly [134] and nonuniformly distorted structures [135]. The B parameter lies in the range between 0.95 and 1.0, which agrees well with physical reasonable bond-length truncation effects in small clusters. Fig. 5.6A shows the distortion function $f(r)$ with different curvature A as a function of r/R. Different distortion functions represent different bond-length distributions of the 1NN bonds or different radial relaxation of the surface tension within a cluster. They calculated the theoretical EXAFS signals in distorted and undistorted clusters and analyzed them using conventional methods, which assume low disorder and include a third cumulant in the analysis. The results exhibited the enhanced surface disorder in metal clusters, in the size range under 5 nm. If such disorder is unaccounted for in the analysis, it may result in the significant underestimation of particle size (Fig. 5.6B) and overestimation of the nearest-neighbor distances. To minimize the errors in the analysis due to the effects of surface relaxation, one can passivate the cluster surface with H_2, which increases bulk-like order in the clusters [105,106,137]. Alternatively, one can take complementary measurements

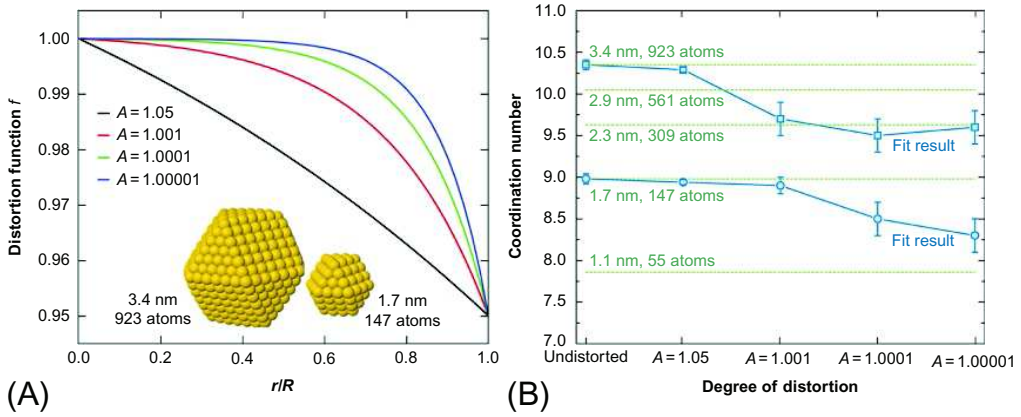

FIG. 5.6 (A) Distortion function with different curvature A as a function of r/R; (B) comparing the modeling 1NN coordination numbers (*horizontal dash lines*) to those obtained by fitting FEFF 6 signal with data generated for model clusters (*symbols*). *(Reproduced with permission from A. Yevick, A.I. Frenkel, Effects of surface disorder on EXAFS modeling of metallic clusters, Phys. Rev. B. 81 (11) (2010) 115451–115453, 115451–115456. Copyright 2010 American Physical Society.)*

using other techniques, in addition to EXAFS, when the asymmetrical disorder causes artifacts in the conventional EXAFS analysis.

Other than the intraparticle disorder, the interparticle disorder also affects the EXAFS results. To investigate the effects of the latter type of disorder, Frenkel et al. [80] averaged the contributions to EXAFS produced by an ensemble of clusters, which are described by a symmetrical distribution ρ of cluster order (L). The latter is approximated as the Gaussian function:

$$\rho(L) = \exp\left(-\frac{(L-\bar{L})^2}{2\sigma_s^2}\right), \tag{5.21}$$

where $\bar{L}$ is the average cluster order and σ_s is the standard deviation in L. The average coordination numbers are calculated over all clusters with the size distribution $\rho(L)$:

$$\tilde{n} = \frac{\int_0^\infty \rho(L)N(L)n(L)dL}{\int_0^\infty \rho(L)N(L)dL}. \tag{5.22}$$

Eq. (5.22) contains a weighting factor, $N(L)$, which indicates the number of atoms in a cluster of the order L. This correction is required because $\rho(L)$ is commonly obtained by EM measurements as a frequency distribution that depends on cluster size, not volume, whereas volume averaging is required for coordination-number measurements by EXAFS. The cluster order L instead of cluster diameter D is employed in Eqs. (5.21), (5.22) to insure that the results are independent of a given material composition. For cuboctahedral clusters, the cluster order L and cluster diameter D are simply related: $D = 2Lr$, where r is the 1NN distance. To estimate the effect of $\rho(L)$ on the average coordination numbers, they assume clusters with cuboctahedral geometry. Accordingly, the calculated average coordination numbers for various values of $\bar{L}$ as a function of σ_s were plotted in Fig. 5.7. If $\sigma_s = 0$ (all clusters are identical), $\tilde{n} = n_0$, the coordination number in each cluster. When σ_s increases, $\tilde{n} > n_0$ because the larger clusters contribute more to the average than do the smaller clusters. For systems with relatively narrow size distribution ($\sigma_s < 0.5$ for small clusters and $\sigma_s < 1$ for larger clusters), the EXAFS predictions are not significantly affected (Fig. 5.7). The 1NN distance r and the Debye-Waller factor σ^2 obtained from EXAFS analysis may be also affected by the distribution of cluster size/order when larger clusters have different spacing between atoms compared with the smaller clusters [80]. Frenkel et al. [80] observed that even for very poorly defined cluster sizes, with $\sigma_s/L \approx 2/3$ and typical choices of $r(L)$, the resulting corrections to r and σ^2 do not exceed 0.015 Å and 0.00015 Å^2, respectively.

In summary, the following guidance can be offered for the interpretation of the coordination numbers in clusters: (1) if the distribution of particles sizes is known, for example, through electron microscopic measurements, the

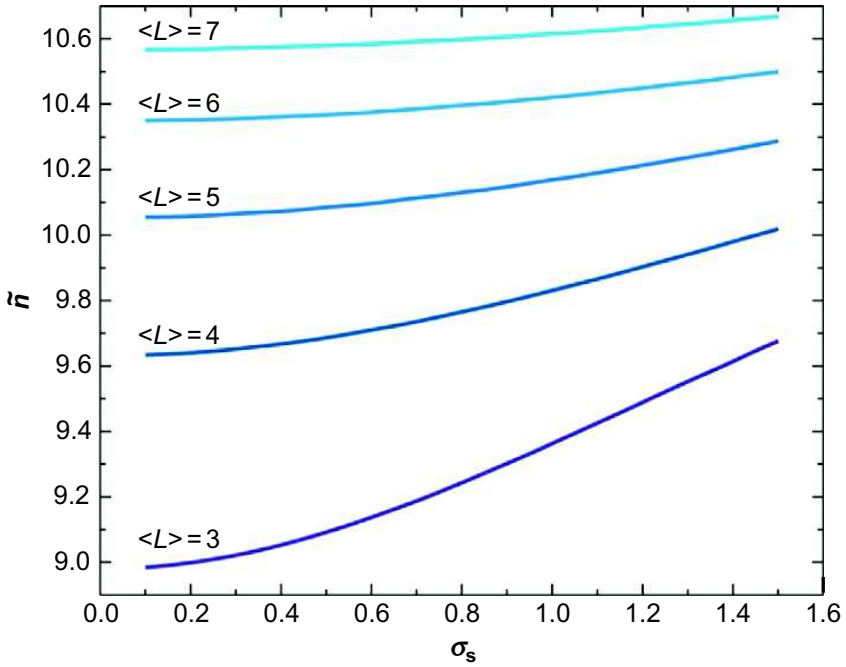

FIG. 5.7 Average coordination number as a function of the standard deviation of the size distribution. *(Reproduced with permission from A.I. Frenkel, A. Yevick, C. Cooper, R. Vasic, Modeling the structure and composition of nanoparticles by extended X-ray absorption fine-structure spectroscopy, Annu. Rev. Anal. Chem. 4 (2011) 34. Copyright 2011 Annual Review.)*

theoretical average coordination number can be obtained by applying Eq. (5.22). (2) For quasi-Gaussian distributions, the average coordination numbers can be determined from Fig. 5.7 for different values of σ_s. (3) If σ_s is incorrectly assumed to be too narrow, the EXAFS coordination numbers overestimate the mean cluster size. (4) The combination of EXAFS and microscopy analyses is necessary in order to find out whether the models proposed on the basis of each method, ones that possess certain sizes and shapes, are in agreement with each other. For example, if the size distribution of the clusters measured in the microscopy experiment brackets the cluster size corresponding to the EXAFS-derived model with specific size and shape, one can conclude that the representative cluster's model resulted from EXAFS is a valid one. (5) The effects of σ_s on the mean bond-length r and its variance σ^2 are relatively weak compared with those on the coordination numbers.

As for the heterometallic clusters, the values of partial coordination numbers are important for analyzing their composition habits. For example, by evaluating the relationship between the partial 1NN coordination numbers and the bulk composition, one can determine whether the nanoalloy is either homogeneous (when average environments around each atom being approximately the same) or heterogeneous (when different regions within the sample have different compositional trends, e.g., A-rich and B-rich or when such segregation occurs within each cluster, e.g., A-rich core and B-rich shell) [79]. However, improper use of the method may lead to wrong conclusions.

We will now focus on random nanoalloys (which have zero short-range order) and highlight challenges in their detection by EXAFS. We now introduce the *total* coordination number of metal-metal pair, n_{MM}, which is equal to n_1 for monometallic clusters. For bulk alloys, when atoms of type A and B are distributed *randomly*, their partial coordination numbers are found from the overall compositions:

$$n_{\mathrm{AA}} = n_{\mathrm{BA}} = x_{\mathrm{A}} n_{\mathrm{MM}}, \quad n_{\mathrm{AB}} = n_{\mathrm{BB}} = (1 - x_{\mathrm{A}})\, n_{\mathrm{MM}}, \tag{5.23}$$

where the composition is defined as $x_{\mathrm{A}} = N_{\mathrm{A}}/N$. Note that in random bulk alloys, $n_{\mathrm{AA}} + n_{\mathrm{BB}} = n_{\mathrm{AA}} + n_{\mathrm{AB}} = n_{\mathrm{BB}} + n_{\mathrm{BA}} = n_{\mathrm{MM}}$. For a nanocluster with random compositional distribution, the equations can be revised and represented as the following [80]:

$$\begin{aligned} n_{\mathrm{AA}} &= \frac{N_{\mathrm{A}} - 1}{N - 1} n_{\mathrm{MM}} = \frac{N x_{\mathrm{A}} - 1}{N - 1} n_{\mathrm{MM}}, \quad n_{\mathrm{AB}} = \frac{N - N_A}{N - 1} n_{\mathrm{MM}} = \frac{N}{N - 1} (1 - x_{\mathrm{A}}) n_{\mathrm{MM}}, \\ n_{\mathrm{BA}} &= \frac{N_A}{N - 1} n_{\mathrm{MM}} = \frac{N}{N - 1} x_{\mathrm{A}}\, n_{\mathrm{MM}}, \quad n_{\mathrm{BB}} = \frac{N_{\mathrm{B}} - 1}{N - 1} n_{\mathrm{MM}} = \left(1 - \frac{N x_{\mathrm{A}}}{N - 1}\right) n_{\mathrm{MM}}. \end{aligned} \tag{5.24}$$

We note that in random nanoalloys, same as in the bulk random alloys, $n_{\mathrm{AA}} + n_{\mathrm{AB}} = n_{\mathrm{BB}} + n_{\mathrm{BA}} = n_{\mathrm{MM}}$, but the sum of n_{AA} and n_{BB} in the nanoalloys is smaller than n_{MM} in bulk:

$$n_{\mathrm{AA}} + n_{\mathrm{BB}} = \frac{N - 2}{N - 1} n_{\mathrm{MM}}. \tag{5.25}$$

Eqs. (5.24), (5.25) are exact, and they are equivalent to Eq. (5.23) in the limit of large total number of atoms (N) and large concentrations (x_{A}). Furthermore, in the random nanoalloys, the n_{AA} and n_{BB} can be different from n_{BA} and n_{AB}, respectively, while in the random bulk alloys, they are the same.

In previous sections, we found that the knowledge of the coordination numbers in heterometallic nanoclusters could be used to determine the size and the clusters' compositional habits, including the degree of the short-range order and the homogeneity of alloying. Here, we discuss the effects of compositional disorder on coordination numbers determined by EXAFS analysis. For demonstration, a simple system that contains clusters of the same size but of different composition is considered. We will assume the distribution of compositions across the ensemble of clusters to be a Gaussian:

$$\rho(x) = \exp\left(-\frac{(x - \bar{x})^2}{2\sigma_c^2}\right), \tag{5.26}$$

where $x = N_{\mathrm{A}}/N$ is the fraction of A atoms in a given cluster, $\bar{x}$ is the average composition over all clusters, and σ_c represents the standard deviation in the

distribution of $\rho(x)$. Furthermore, assuming a random ordering of the atoms within each cluster, the partial coordination number n_{AA} in each cluster is defined as

$$n_{AA} = \frac{N_A - 1}{N - 1} n_{MM}, \tag{5.27}$$

where N_A is the number of A atoms in the given cluster and N is the total number of atoms in each cluster and is identical for all clusters as a result of the identical cluster size. Compared with the equations used by Hwang et al. [138] and Frenkel [79] that require that $n_{AA} = x n_{MM}$ for randomly distributed atoms within the clusters, Eq. (5.27) is more general and accurate for all clusters and correctly calculates the coordination numbers over the entire compositional range. The exact formulas for the partial coordination numbers, averaged over the ensemble of clusters, are

$$\widetilde{n}_{AA} = \frac{\int_0^1 \rho(x) x n_{AA}(x) dx}{\int_0^1 \rho(x) x dx} \tag{5.28}$$

and

$$\widetilde{n}_{AB} = n_{MM} - \widetilde{n}_{AA} = n_{AM} - \widetilde{n}_{AA}. \tag{5.29}$$

For clusters with $N = 100$ atoms, calculated partial coordination numbers that have been normalized by n_{MM} are shown in Fig. 5.8. The results

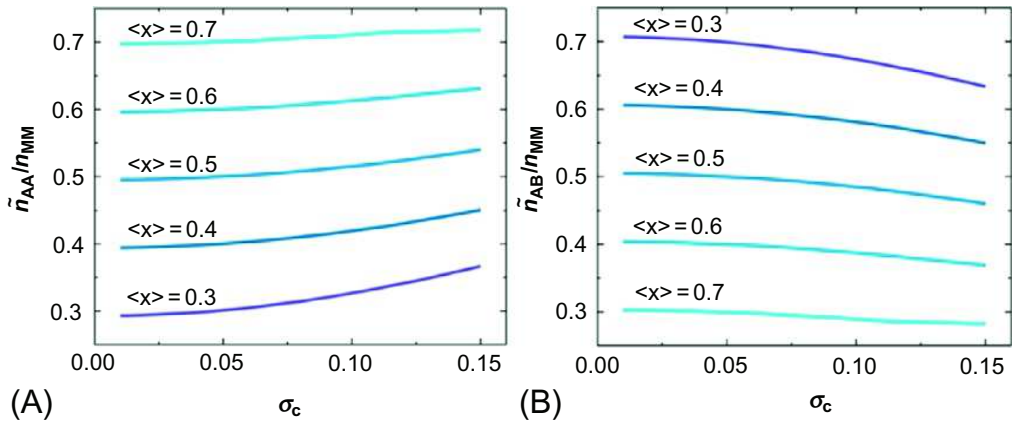

FIG. 5.8 Normalized partial coordination numbers of (A) AA and (B) AB pairs as functions of the standard deviation σ_c around the average cluster composition $\langle x \rangle$ for clusters of $N = 100$ atoms, calculated assuming a Gaussian compositional distribution. In both figures, cartoons next to the $\langle x \rangle = 0.5$ curve illustrate the difference between the narrow (*one cluster on the left*) and broad (*three different clusters on the right*) compositional distributions. *(Reproduced with permission from A.I. Frenkel, A. Yevick, C. Cooper, R. Vasic, Modeling the structure and composition of nanoparticles by extended X-ray absorption fine-structure spectroscopy, Annu. Rev. Anal. Chem. 4 (2011) 36. Copyright 2011 Annual Review.)*

indicate that the ensemble average coordination number $\tilde{n}_{AA}$ can be smaller for narrow compositional distributions or larger for broad distributions than the coordination numbers predicted by the equation $n_{AA} = xn_{MM}$. The two sets of values, $\tilde{n}_{AA}$ and n_{AA}, agree for $\sigma_c = \sqrt{x(1-x)/N}$, for which the normal distribution coincides with binomial distribution.

In summary of this part, we remark that the narrow distributions of cluster sizes and compositions across the ensemble of clusters in the sample are crucial for accurate characterization of intraparticle composition in bimetallic systems. In case the distributions are not narrow, corrective strategies are possible when prior knowledge or the width of the distributions exists from complementary studies.

5.3 OUTLOOK AND PERSPECTIVES

As shown throughout this chapter, EXAFS possesses excellent spatial resolution to probe atomic architecture in nanoscale metal clusters. It demonstrates the best quantitative powers when the distribution of cluster sizes, shapes, and compositions is narrow and the interatomic distances are symmetrically distributed around an average value. In that case, the model of a representative cluster will emerge from the analysis of the EXAFS data, where unique details of structural and compositional motifs can be obtained.

We have also demonstrated the limitation in the analysis and modeling of EXAFS data in clusters due to the ensemble-averaging nature of the EXAFS technique. If the distribution of particles is broad, results of the measurements cannot be simply interpreted in terms of a "mean" particle due to a number of simplifying assumptions made in EXAFS data analysis. A possible remedy toward a more accurate analysis of individual clusters, not relying on the average over the ensemble, is single nanoparticle spectroscopy [139–143]. Hitchcock and Toney recently published an overview of spectromicroscopy methods that include nanoprobe-based systems [144]. As an illustration of the capability of nanoprobe methods in studies of single nanoparticles, Chu's group used scanning multilayer Laue lens X-ray microscopy to study the oxidation process of individual PtNi nanoparticles [145]. Frenkel and van Bokhoven reviewed major challenges for the existing nanospectroscopic methods. They suggested the following three directions for advancing the XAFS spectroscopy toward the single nanoparticle level [146]: (1) decrease the spot size to well below 10 nm while maintaining sufficiently high flux to probe individual nanoparticles of interest, (2) enable energy scanning while maintaining the spot size and position, and (3) study materials that change in the process of their work, which demands that the single-particle spectroscopy at the nanometer level should be performed in operando conditions.

The latter challenge is directly related to one of the most important requirements to modern applications of synchrotron-based spectroscopic methods, that is, to characterize nanoclusters in situ, where the nanoclusters

are studied as a function of temperature, pressure, or time [28,147,82,148], and/or investigate the work mechanism of nanocatalysts in operando conditions [115,149]. Accordingly, there are growing demands in developing time-resolved and operando techniques. Extensive efforts have been made in this regard. For instance, Stach and Frenkel et al. recently demonstrated the advantage of using a microreactor for nanocatalysis studies at ambient temperature and pressure [115,150], by bridging the "pressure gas" between spectroscopic and electron microscopic techniques. The catalytically active site is often only a minority of atoms in the catalysts; sensitivity is therefore an issue. Ferri et al. employed modulation excitation method [151–153], which provides better sensitivity to the structure of the catalytically active site [152,154]. Pump-probe measurements are able to capture structural variation at the micro-, nano-, pico-, and even femtosecond time scales [155]. In the literature related to this technique, most of them are about photocatalytic process during which a flash of light induces electron excitation after which a structure change occurs and detected in the ultrafast time domain [156,157].

To summarize, nanoclusters have been studied for several decades with increasing accuracy and level of detail that parallel the development of analytic methods. Of those methods, XAS technique proved to be uniquely capable to capture multiple attributes of structure, such as the size, shape, surface relaxation, and compositional motifs, and measure their dynamic changes in real time due to externally controlled conditions. The combination of the ongoing developments of cluster synthesis methods, new synchrotron nanoprobe methodologies, and the increased use of in situ/operando characterization techniques are the promising new directions toward future progress in this field in the next decade.

ACKNOWLEDGMENTS

A.I. Frenkel acknowledges funding of this work by the Division of Chemical Sciences, Geosciences, and Biosciences within the US Department of Energy Office of Basic Energy Sciences, Grant No. DE-FG02-03ER15476. Q. Wang acknowledges support from the Catalysis Center for Energy Innovation, an Energy Frontier Research Center funded by the US Department of Energy Office of Science and Office of Basic Energy Sciences under Award DE-SC0001004.

REFERENCES

[1] R.L. Johnston, Atomic and Molecular Clusters, Taylor & Francis, London, 2002.
[2] J. Zheng, P.R. Nicovich, R.M. Dickson, Highly fluorescent noble-metal quantum dots, Annu. Rev. Phys. Chem. 58 (1) (2007) 409–431.
[3] O.M. Bakr, V. Amendola, C.M. Aikens, W. Wenseleers, R. Li, L. Dal Negro, et al., Silver nanoparticles with broad multiband linear optical absorption, Angew. Chem. Int. Ed. 48 (32) (2009) 5921–5926.

[4] C.-A.J. Lin, T.-Y. Yang, C.-H. Lee, S.H. Huang, R.A. Sperling, M. Zanella, et al., Synthesis, characterization, and bioconjugation of fluorescent gold nanoclusters toward biological labeling applications, ACS Nano 3 (2) (2009) 395–401.
[5] J. Jortner, Cluster size effects, Z. Phys. D: At. Mol. Clusters 24 (3) (1992) 247–275.
[6] Z.Y. Li, N.P. Young, M. Di Vece, S. Palomba, R.E. Palmer, A.L. Bleloch, et al., Three-dimensional atomic-scale structure of size-selected gold nanoclusters, Nature 451 (7174) (2008) 46–48.
[7] C.Q. Sun, Y. Wang, B.K. Tay, S. Li, H. Huang, Y.B. Zhang, Correlation between the melting point of a nanosolid and the cohesive energy of a surface atom, J. Phys. Chem. B 106 (41) (2002) 10701–10705.
[8] M.W. Small, S.I. Sanchez, N.S. Marinkovic, A.I. Frenkel, R.G. Nuzzo, Influence of adsorbates on the electronic structure, bond strain, and thermal properties of an alumina-supported Pt catalyst, ACS Nano 6 (6) (2012) 5583–5595.
[9] A.I. Frenkel, M.W. Small, J.G. Smith, R.G. Nuzzo, K.O. Kvashnina, M. Tromp, An in situ study of bond strains in 1 nm Pt catalysts and their sensitivities to cluster–support and cluster–adsorbate interactions, J. Phys. Chem. C 117 (44) (2013) 23286–23294.
[10] M.W. Small, J.J. Kas, K.O. Kvashnina, J.J. Rehr, R.G. Nuzzo, M. Tromp, et al., Effects of adsorbate coverage and bond-length disorder on the d-band center of carbon-supported Pt catalysts, ChemPhysChem 15 (8) (2014) 1569–1572.
[11] E.C. Tyo, S. Vajda, Catalysis by clusters with precise numbers of atoms, Nat. Nanotechnol. 10 (7) (2015) 577–588.
[12] U. Landman, W.D. Luedtke, Small is different: energetic, structural, thermal, and mechanical properties of passivated nanocluster assemblies, Faraday Discuss. 125 (2004) 1–22.
[13] B.C. Gates, Supported metal clusters: synthesis, structure, and catalysis, Chem. Rev. 95 (3) (1995) 511–522.
[14] H. Zheng, R.K. Smith, Y.-W. Jun, C. Kisielowski, U. Dahmen, A.P. Alivisatos, Observation of single colloidal platinum nanocrystal growth trajectories, Science 324 (5932) (2009) 1309–1312.
[15] S. Helveg, C. Lopez-Cartes, J. Sehested, P.L. Hansen, B.S. Clausen, J.R. Rostrup-Nielsen, et al., Atomic-scale imaging of carbon nanofibre growth, Nature 427 (6973) (2004) 426–429.
[16] P.L. Hansen, J.B. Wagner, S. Helveg, J.R. Rostrup-Nielsen, B.S. Clausen, H. Topsøe, Atom-resolved imaging of dynamic shape changes in supported copper nanocrystals, Science 295 (5562) (2002) 2053–2055.
[17] E.A. Stach, R. Hull, R.M. Tromp, F.M. Ross, M.C. Reuter, J.C. Bean, In-situ transmission electron microscopy studies of the interaction between dislocations in strained SiGe/Si(001) heterostructures, Philos. Mag. A 80 (9) (2000) 2159–2200.
[18] S.I. Sanchez, M.W. Small, J. Zuo, R.G. Nuzzo, Structural characterization of Pt–Pd and Pd–Pt core–shell nanoclusters at atomic resolution, J. Am. Chem. Soc. 131 (24) (2009) 8683–8689.
[19] M.W. Small, S. Sanchez, L. Menard, J.H. Kang, A.I. Frenkel, R.G. Nuzzo, The atomic structural dynamics of γ-Al_2O_3 supported Ir–Pt nanocluster catalysts prepared from a bimetallic molecular precursor: a study using aberration-corrected electron microscopy and X-ray absorption spectroscopy, J. Am. Chem. Soc. 133 (10) (2011) 3582–3591.
[20] H. Yoshida, Y. Kuwauchi, J. Jinschek, K. Sun, S. Tanaka, M. Kohyama, et al., Visualizing gas molecules interacting with supported nanoparticulate catalysts at reaction conditions, Science 335 (2012) 317–326.

[21] J.C. Yang, M.W. Small, R.V. Grieshaber, R.G. Nuzzo, Recent developments and applications of electron microscopy to heterogeneous catalysis, Chem. Soc. Rev. 41 (24) (2012) 8179–8194.
[22] W.E. Kaden, T. Wu, W.A. Kunkel, S.L. Anderson, Electronic structure controls reactivity of size-selected Pd clusters adsorbed on TiO_2 surfaces, Science 326 (5954) (2009) 826–829.
[23] F. Tao, M.E. Grass, Y. Zhang, D.R. Butcher, J.R. Renzas, Z. Liu, et al., Reaction-driven restructuring of Rh-Pd and Pt-Pd core-shell nanoparticles, Science 322 (5903) (2008) 932–934.
[24] K. Sasaki, K.A. Kuttiyiel, L. Barrio, D. Su, A.I. Frenkel, N. Marinkovic, et al., Carbon-supported IrNi core–shell nanoparticles: synthesis, characterization, and catalytic activity, J. Phys. Chem. C 115 (20) (2011) 9894–9902.
[25] M.A. Brown, I. Jordan, A. Beloqui Redondo, A. Kleibert, H.J. Wörner, J.A. van Bokhoven, In situ photoelectron spectroscopy at the liquid/nanoparticle interface, Surf. Sci. 610 (2013) 1–6.
[26] A. Agbabiaka, M. Wiltfong, C. Park, Small angle X-ray scattering technique for the particle size distribution of nonporous nanoparticles, J. Nanoparticles 2013 (2013) 11.
[27] S.J.L. Billinge, I. Levin, The problem with determining atomic structure at the nanoscale, Science 316 (5824) (2007) 561–565.
[28] A.I. Frenkel, J.A. Rodriguez, J.G. Chen, Synchrotron techniques for in situ catalytic studies: capabilities, challenges, and opportunities, ACS Catal. 2 (11) (2012) 2269–2280.
[29] A.M. Beale, A.M. van der Eerden, K. Kervinen, M.A. Newton, B.M. Weckhuysen, Adding a third dimension to operando spectroscopy: a combined UV–vis, Raman and XAFS setup to study heterogeneous catalysts under working conditions, Chem. Commun. (24) (2005) 3015–3017.
[30] S.J. Tinnemans, J.G. Mesu, K. Kervinen, T. Visser, T.A. Nijhuis, A.M. Beale, et al., Combining operando techniques in one spectroscopic-reaction cell: new opportunities for elucidating the active site and related reaction mechanism in catalysis, Catal. Today 113 (1–2) (2006) 3–15.
[31] B.M. Weckhuysen, Determining the active site in a catalytic process: operando spectroscopy is more than a buzzword, Phys. Chem. Chem. Phys. 5 (20) (2003) 4351–4360.
[32] A. Tilekaratne, J.P. Simonovis, M.F.L. Fagúndez, M. Ebrahimi, F. Zaera, Operando studies of the catalytic hydrogenation of ethylene on Pt(111) single crystal surfaces, ACS Catal. 2 (2012) 10.
[33] G. Nurk, T. Huthwelker, A. Braun, C. Ludwig, E. Lust, R.P.W.J. Struis, Redox dynamics of sulphur with Ni/GDC anode during SOFC operation at mid- and low-range temperatures: an operando S K-edge XANES study, J. Power Sources 240 (2013) 10.
[34] H. Topsøe, Developments in operando studies and in situ characterization of heterogeneous catalysts, J. Catal. 216 (2003) 10.
[35] J.A. Rodriguez, J.C. Hanson, D. Stacchiola, S.D. Senanayake, In situ/operando studies for the production of hydrogen through the water-gas shift on metal oxide catalysts, Phys. Chem. Chem. Phys. 15 (2013) 12004–12025.
[36] A. Patlolla, E.V. Carino, S.N. Ehrlich, E. Stavitski, A.I. Frenkel, Application of operando XAS, XRD, and Raman spectroscopy for phase speciation in water gas shift reaction catalysts, ACS Catal. 2 (11) (2012) 2216–2223.
[37] M.G. Weir, V.S. Myers, A.I. Frenkel, R.M. Crooks, In situ X-ray absorption analysis of similar to 1.8 nm dendrimer-encapsulated Pt nanoparticles during electrochemical CO oxidation, ChemPhysChem 11 (13) (2010) 2942–2950.

[38] F. Tao, Operando studies of catalyst surfaces during catalysis and under reaction conditions: ambient pressure X-ray photoelectron spectroscopy with a flow-cell reactor, ChemCatChem 4 (2012) 8.
[39] S.J. Kweskin, R.M. Rioux, H. Song, K. Komvopoulos, P. Yang, G.A. Somorjai, High-pressure adsorption of ethylene on cubic Pt nanoparticles and Pt(100) single crystals probed by in situ sum frequency generation vibrational spectroscopy, ACS Catal. 2 (2012) 10.
[40] J.C. Fierro-Gonzalez, J. Guzman, B.C. Gates, Role of cationic gold in supported CO oxidation catalysts, Top. Catal. 44 (1–2) (2007) 12.
[41] X. Nie, H. Qian, Q. Ge, H. Xu, R. Jin, CO oxidation catalyzed by oxide-supported Au25 (SR)18 nanoclusters and identification of perimeter sites as active centers, ACS Nano 6 (7) (2012) 9.
[42] C. Louis, C. Lepetit, M. Che, EPR characterization of oxide supported transition metal ions: relevance to catalysis, Mol. Eng. 4 (1–3) (1994) 35.
[43] K. Shimizu, K. Sugino, K. Kato, S. Yokota, K. Okumura, A. Satsuma, Formation and redispersion of silver clusters in Ag-MFI zeolite as investigated by time-resolved QXAFS and UV–vis, J. Phys. Chem. C 111 (2007) 6.
[44] M. Høj, A.D. Jensen, J.-D. Grunwald, Structure of alumina supported vanadia catalysts for oxidative dehydrogenation of propane prepared by flame spray pyrolysis, Appl. Catal. A 451 (2013) 8.
[45] E. Stavitski, B.M. Weckhuysen, Infrared and Raman imaging of heterogeneous catalysts, Chem. Soc. Rev. 39 (12) (2010) 4615–4625.
[46] G. Rupprechter, A surface science approach to ambient pressure catalytic reactions, Catal. Today 126 (2007) 15.
[47] A.J. Dent, Development of time-resolved XAFS instrumentation for quick EXAFS and energy-dispersive EXAFS measurements on catalyst systems, Top. Catal. 18 (1–2) (2002) 27–35.
[48] T.T. Fister, G.T. Seidler, L. Wharton, A.R. Battle, T.B. Ellis, J.O. Cross, et al., Multielement spectrometer for efficient measurement of the momentum transfer dependence of inelastic X-ray scattering, Rev. Sci. Instrum. 77 (6) (2006) 063901.
[49] T.T. Fister, M. Schmidt, P. Fenter, C.S. Johnson, M.D. Slater, M.K.Y. Chan, et al., Electronic structure of lithium battery interphase compounds: comparison between inelastic X-ray scattering measurements and theory, J. Chem. Phys. 135 (22) (2011) 224513.
[50] M. Tromp, J.A. van Bokhoven, O.V. Safonova, F.M.F.D. Groot, J. Evans, P. Glatzel, High energy resolution fluorescence detection X-ray absorption spectroscopy: detection of adsorption sites in supported metal catalysts, AIP Conf. Proc. 882 (1) (2007) 651–653.
[51] J.A. van Bokhoven, C. Louis, J.T. Miller, M. Tromp, O.V. Safonova, P. Glatzel, Activation of oxygen on gold/alumina catalysts: in situ high-energy-resolution fluorescence and time-resolved X-ray spectroscopy, Angew. Chem. Int. Ed. 118 (28) (2006) 4767–4770.
[52] A.I. Frenkel, M.W. Cason, A. Elsen, U. Jung, M.W. Small, R.G. Nuzzo, et al., Critical review: effects of complex interactions on structure and dynamics of supported metal catalysts, J. Vac. Sci. Technol. A 32 (2) (2014) 020801.
[53] D.E. Sayers, E.A. Stern, F.W. Lytle, New technique for investigating noncrystalline structures: fourier analysis of the extended X-ray absorption fine structure, Phys. Rev. Lett. 27 (18) (1971) 1204–1207.
[54] S.I. Zabinsky, J.J. Rehr, A. Ankudinov, R.C. Albers, M.J. Eller, Multiple-scattering calculations of X-ray-absorption spectra, Phys. Rev. B 52 (4) (1995) 2995–3009.
[55] G. Bunker, Application of the ratio method of EXAFS analysis to disordered systems, Nucl. Instrum. Methods Phys. Res. 207 (1983) 437–444.

[56] J.J. Rehr, R.C. Albers, Theoretical approaches to X-ray absorption fine structure, Rev. Mod. Phys. 72 (2000) 621–654.
[57] A.L. Ankudinov, B. Ravel, J.J. Rehr, S.D. Conradson, Real-space multiple-scattering calculation and interpretation of X-ray-absorption near-edge structure, Phys. Rev. B 58 (12) (1998) 7565–7576.
[58] J.J. Rehr, J.J. Kas, M.P. Prange, A.P. Sorini, Y. Takimoto, F. Vila, Ab initio theory and calculations of X-ray spectra, C. R. Phys. 10 (2009) 548–559.
[59] S.J. Gurman, N. Binsted, I. Ross, A rapid, exact curved-wave theory for EXAFS calculations, J. Phys. C Solid State Phys. 17 (1) (1984) 143–151.
[60] A. Filipponi, A.D. Cicco, C.R. Natoli, X-ray-absorption spectroscopy and n-body distribution functions in condensed matter. I. Theory, Phys. Rev. B 52 (21) (1995) 15122–15134.
[61] S.R. Bare, G.E. Mickelson, F.S. Modica, A.Z. Ringwelski, N. Yang, Simple flow through reaction cells for in situ transmission and fluorescence X-ray-absorption spectroscopy of heterogeneous catalysts, Rev. Sci. Instrum. 77 (2) (2006) 023105.
[62] S.R. Bare, N. Yang, S.D. Kelly, G.E. Mickelson, F.S. Modica, Design and operation of a high pressure reaction cell for in situ X-ray absorption spectroscopy, Catal. Today 126 (1–2) (2007) 18–26.
[63] E.M. Erickson, M.S. Thorum, R. Vasić, N.S. Marinković, A.I. Frenkel, A.A. Gewirth, et al., In situ electrochemical X-ray absorption spectroscopy of oxygen reduction electrocatalysis with high oxygen flux, J. Am. Chem. Soc. 134 (1) (2011) 197–200.
[64] J.D. Grunwaldt, M. Caravati, S. Hannemann, A. Baiker, X-ray absorption spectroscopy under reaction conditions: suitability of different reaction cells for combined catalyst characterization and time-resolved studies, Phys. Chem. Chem. Phys. 6 (11) (2004) 3037–3047.
[65] J. McBreen, W.E. O'Grady, K.I. Pandya, R.W. Hoffman, D.E. Sayers, EXAFS study of the nickel oxide electrode, Langmuir 3 (3) (1987) 428–433.
[66] M.S. Nashner, A.I. Frenkel, D.L. Adler, J.R. Shapley, R.G. Nuzzo, Structural characterization of carbon-supported platinum–ruthenium nanoparticles from the molecular cluster precursor PtRu5C(CO)16, J. Am. Chem. Soc. 119 (33) (1997) 7760–7771.
[67] K. Sasaki, J. Zhang, J. Wang, F. Uribe, R. Adzic, Platinum submonolayer-monolayer electrocatalysis: an electrochemical and X-ray absorption spectroscopy study, Res. Chem. Intermed. 32 (5) (2006) 543–559.
[68] R. Viswanathan, R. Liu, E.S. Smotkin, In situ X-ray absorption fuel cell, Rev. Sci. Instrum. 73 (5) (2002) 2124–2127.
[69] R.J.K. Wiltshire, C.R. King, A. Rose, P.P. Wells, M.P. Hogarth, D. Thompsett, et al., A PEM fuel cell for in situ XAS studies, Electrochim. Acta 50 (25–26) (2005) 5208–5217.
[70] Y. Uemura, Y. Inada, K.K. Bando, T. Sasaki, N. Kamiuchi, K. Eguchi, et al., In situ time-resolved XAFS study on the structural transformation and phase separation of Pt3Sn and PtSn alloy nanoparticles on carbon in the oxidation process, Phys. Chem. Chem. Phys. 13 (2011) 12.
[71] E.D. Crozier, A review of the current status of XAFS spectroscopy, Nucl. Inst. Methods Phys. Res. B 133 (1–4) (1997) 134–144.
[72] G. Bunker, A Practical Guide to X-ray Absorption Fine Structure Spectroscopy, Cambridge University Press, Cambridge, 2010.
[73] J.A. Penner-Hahn, X-ray absorption spectroscopy in coordination chemistry, Coord. Chem. Rev. 190–192 (1999) 1101–1123.
[74] E.A. Stern, S.M. Heald, Basic principles and applications of EXAFS, in: E.E. Koch (Ed.), Handbook of Synchrotron Radiation, North-Holland, New York, NY, 1983, pp. 995–1014.

[75] H. Wende, Recent advances in X-ray absorption spectroscopy, Rep. Prog. Phys. 67 (12) (2004) 2105.
[76] M.S. Nashner, A.I. Frenkel, D. Somerville, C.W. Hills, J.R. Shapley, R.G. Nuzzo, Core shell inversion during nucleation and growth of bimetallic Pt/Ru nanoparticles, J. Am. Chem. Soc. 120 (32) (1998) 8093–8101.
[77] A.I. Frenkel, Solving the structure of nanoparticles by multiple-scattering EXAFS analysis, J. Synchrotron Radiat. 6 (3) (1999) 293–295.
[78] A.I. Frenkel, C.W. Hills, R.G. Nuzzo, A view from the inside: complexity in the atomic scale ordering of supported metal nanoparticles, J. Phys. Chem. B 105 (51) (2001) 12689–12703.
[79] A. Frenkel, Solving the 3D structure of metal nanoparticles, Z. Krist. 222 (11/2007) (2007) 605–611.
[80] A.I. Frenkel, A. Yevick, C. Cooper, R. Vasic, Modeling the structure and composition of nanoparticles by extended X-ray absorption fine-structure spectroscopy, Annu. Rev. Anal. Chem. 4 (2011) 23–39.
[81] A.E. Russell, A. Rose, X-ray absorption spectroscopy of low temperature fuel cell catalysts, Chem. Rev. 104 (10) (2004) 4613–4636.
[82] J. Singh, C. Lamberti, J.A. van Bokhoven, Advanced X-ray absorption and emission spectroscopy: in situ catalytic studies, Chem. Soc. Rev. 39 (12) (2010) 4754–4766.
[83] H. Modrow, Tuning nanoparticle properties—the X-ray absorption spectroscopic point of view, Appl. Spectrosc. Rev. 39 (2) (2004) 183–290.
[84] A.I. Frenkel, Applications of extended X-ray absorption fine-structure spectroscopy to studies of bimetallic nanoparticle catalysts, Chem. Soc. Rev. 41 (24) (2012) 8163–8178.
[85] P.A. Lee, P.H. Citrin, P. Eisenberger, B.M. Kincaid, Extended X-ray absorption fine structure—its strengths and limitations as a structural tool, Rev. Mod. Phys. 53 (4) (1981) 769–806.
[86] A.G. McKale, B.W. Veal, A.P. Paulikas, S.K. Chan, G.S. Knapp, Generalized Ramsauer-Townsend effect in extended X-ray-absorption fine structure, Phys. Rev. B 38 (15) (1988) 10919–10921.
[87] J.J. Rehr, C.H. Booth, F. Bridges, S.I. Zabinsky, X-ray-absorption fine structure in embedded atoms, Phys. Rev. B 49 (17) (1994) 12347–12350.
[88] J.M. Montejano-Carrizales, F. Aguilera-Granja, J.L. Morán-López, Direct enumeration of the geometrical characteristics of clusters, Nanostruct. Mater. 8 (3) (1997) 269–287.
[89] J.M. Montejano-Carrizales, J.L. Morán-López, Geometrical characteristics of compact nanoclusters, Nanostruct. Mater. 1 (5) (1992) 397–409.
[90] D. Glasner, A.I. Frenkel, Geometrical characteristics of regular polyhedra: application to EXAFS studies of nanoclusters, AIP Conf. Proc. 882 (1) (2007) 746–748.
[91] Y. Li, D. Zakharov, S. Zhao, R. Tappero, U. Jung, A. Elsen, et al., Complex structural dynamics of nanocatalysts revealed in operando conditions by correlated imaging and spectroscopy probes, Nat. Commun. 6 (2015) 7583.
[92] S. Calvin, M.M. Miller, R. Goswami, S.-F. Cheng, S.P. Mulvaney, L.J. Whitman, et al., Determination of crystallite size in a magnetic nanocomposite using extended X-ray absorption fine structure, J. Appl. Phys. 94 (1) (2003) 778–783.
[93] A.I. Frenkel, S.C. Frankel, T. Liu, Structural stability of giant polyoxomolybdate molecules as probed by EXAFS, Phys. Scr. 2005 (T115) (2005) 721.
[94] B. Roldan Cuenya, J.R. Croy, S. Mostafa, F. Behafarid, L. Li, Z. Zhang, et al., Solving the structure of size-selected Pt nanocatalysts synthesized by inverse Micelle encapsulation, J. Am. Chem. Soc. 132 (25) (2010) 8747–8756.

[95] L.D. Menard, H. Xu, S.-P. Gao, R.D. Twesten, A.S. Harper, Y. Song, et al., Metal core bonding motifs of monodisperse icosahedral Au13 and larger Au monolayer-protected clusters as revealed by X-ray absorption spectroscopy and transmission electron microscopy, J. Phys. Chem. B 110 (30) (2006) 14564–14573.

[96] A.I. Frenkel, L.D. Menard, P. Northrup, J.A. Rodriguez, F. Zypman, D. Glasner, et al., Geometry and charge state of mixed-ligand Au13 nanoclusters, AIP Conf. Proc. 882 (1) (2007) 749–751.

[97] B.R. Cuenya, J.R. Croy, S. Mostafa, F. Behafarid, L. Li, Z. Zhang, et al., Solving the structure of size-selected Pt nanocatalysts synthesized by inverse micelle encapsulation, J. Am. Chem. Soc. 132 (25) (2010) 8747–8756.

[98] S. Mostafa, F. Behafarid, J.R. Croy, L.K. Ono, L. Li, J.C. Yang, et al., Shape-dependent catalytic properties of Pt nanoparticles, J. Am. Chem. Soc. 132 (44) (2010) 15714–15719.

[99] A. Jentys, Estimation of mean size and shape of small metal particles by EXAFS, Phys. Chem. Chem. Phys. 1 (17) (1999) 4059–4063.

[100] A.M. Beale, B.M. Weckhuysen, EXAFS as a tool to interrogate the size and shape of mono and bimetallic catalyst nanoparticles, Phys. Chem. Chem. Phys. 12 (21) (2010) 5562–5574.

[101] E.M. Erickson, M.E. Oruc, D.J. Wetzel, M.W. Cason, T.T.H. Hoang, M.W. Small, et al., A comparison of atomistic and continuum approaches to the study of bonding dynamics in electrocatalysis: microcantilever stress and in situ EXAFS observations of platinum bond expansion due to oxygen adsorption during the oxygen reduction reaction, Anal. Chem. 86 (16) (2014) 8368–8375.

[102] A. Frenkel, E. Stern, A. Voronel, S. Heald, Lattice strains in disordered mixed salts, Solid State Commun. 99 (2) (1996) 67–71.

[103] Y. Rosenberg, V.S. Machavariani, A. Voronel, S. Garber, A. Rubshtein, A.I. Frenkel, et al., Strain energy density in the X-ray powder diffraction from mixed crystals and alloys, J. Phys. Condens. Matter 12 (37) (2000) 8081.

[104] V.S. Machavariani, Y. Rosenberg, A. Voronel, S. Garber, A. Rubstein, A.I. Frenkel, et al., Local disorder in mixed crystals as viewed by XRPD, AIP Conf. Proc. 554 (1) (2001) 521–524.

[105] J.H. Kang, L.D. Menard, R.G. Nuzzo, A.I. Frenkel, Unusual non-bulk properties in nanoscale materials: thermal metal–metal bond contraction of γ-alumina-supported Pt catalysts, J. Am. Chem. Soc. 128 (37) (2006) 12068–12069.

[106] S.I. Sanchez, L.D. Menard, A. Bram, J.H. Kang, M.W. Small, R.G. Nuzzo, et al., The emergence of nonbulk properties in supported metal clusters: negative thermal expansion and atomic disorder in Pt nanoclusters supported on γ-Al_2O_3, J. Am. Chem. Soc. 131 (20) (2009) 7040–7054.

[107] C.W. Mays, J.S. Vermaak, D. Kuhlmann-Wilsdorf, On surface stress and surface tension: II. Determination of the surface stress of gold, Surf. Sci. 12 (2) (1968) 134–140.

[108] A.I. Frenkel, S. Nemzer, I. Pister, L. Soussan, T. Harris, Y. Sun, et al., Size-controlled synthesis and characterization of thiol-stabilized gold nanoparticles, J. Chem. Phys. 123 (18) (2005) 184701.

[109] J. Rockenberger, L. Tröger, A. Kornowski, T. Voßmeyer, A. Eychmüller, J. Feldhaus, et al., Size dependence of structural and dynamic properties of CdS-nanoparticles, Ber. Bunsen Ges. 101 (11) (1997) 1613–1616.

[110] R. Xia, J.L. Wang, R. Wang, X. Li, X. Zhang, X.-Q. Feng, et al., Correlation of the thermal and electrical conductivities of nanoporous gold, Nanotechnology 21 (2010) 085703.

[111] A.I. Frenkel, R. Vasic, B. Dukesz, D. Li, M.W. Chen, L. Zhang, et al., Thermal properties of nanoporous gold, Phys. Rev. B 85 (2012) 195419.

[112] J.H. Hodak, A. Henglein, G.V. Hartland, Size dependent properties of Au particles: coherent excitation and dephasing of acoustic vibrational modes, J. Chem. Phys. 111 (18) (1999) 8613–8621.
[113] X. Zhou, W. Xu, G. Liu, D. Panda, P. Chen, Size-dependent catalytic activity and dynamics of gold nanoparticles at the single-molecule level, J. Am. Chem. Soc. 132 (1) (2009) 138–146.
[114] K.P. McKenna, A.L. Shluger, Shaping the morphology of gold nanoparticles by CO adsorption, J. Phys. Chem. C 111 (51) (2007) 18848–18852.
[115] H. Liu, W. An, Y. Li, A.I. Frenkel, K. Sasaki, C. Koenigsmann, et al., In situ probing of the active site geometry of ultrathin nanowires for the oxygen reduction reaction, J. Am. Chem. Soc. 137 (39) (2015) 12597–12609.
[116] W. Liu, P. Rodriguez, L. Borchardt, A. Foelske, J. Yuan, A.-K. Herrmann, et al., Bimetallic aerogels: high-performance electrocatalysts for the oxygen reduction reaction, Angew. Chem. Int. Ed. 52 (37) (2013) 9849–9852.
[117] S. Sun, C.B. Murray, D. Weller, L. Folks, A. Moser, Monodisperse FePt nanoparticles and ferromagnetic FePt nanocrystal superlattices, Science 287 (5460) (2000) 1989–1992.
[118] J.-I. Park, M.G. Kim, Y.-W. Jun, J.S. Lee, W.-R. Lee, J. Cheon, Characterization of superparamagnetic "core–shell" nanoparticles and monitoring their anisotropic phase transition to ferromagnetic "solid solution" nanoalloys, J. Am. Chem. Soc. 126 (29) (2004) 9072–9078.
[119] S.R. Nicewarner-Peña, R.G. Freeman, B.D. Reiss, L. He, D.J. Peña, I.D. Walton, et al., Submicrometer metallic barcodes, Science 294 (5540) (2001) 137–141.
[120] M. Ganguly, A. Pal, Y. Negishi, T. Pal, Synthesis of highly fluorescent silver clusters on gold(I) surface, Langmuir 29 (6) (2013) 2033–2043.
[121] A.I. Frenkel, Q. Wang, S.I. Sanchez, M.W. Small, R.G. Nuzzo, Short range order in bimetallic nanoalloys: an extended X-ray absorption fine structure study, J. Chem. Phys. 138 (6) (2013) 064202.
[122] J.M. Cowley, An approximate theory of order in alloys, Phys. Rev. 77 (5) (1950) 669–675.
[123] J.M. Cowley, Short- and long-range order parameters in disordered solid solutions, Phys. Rev. 120 (5) (1960) 1648–1657.
[124] J.M. Cowley, Short-range order and long-range order parameters, Phys. Rev. 138 (5A) (1965) A1384–A1389.
[125] W.R. Flavell, M. Mian, A.J. Roberts, J.F. Howlett, M.M. Sarker, P.L. Wincott, et al., EXAFS studies of SrSn1-xSbxO3 and BaPb1-xBixO3, J. Mater. Chem. 7 (2) (1997) 357–364.
[126] C.G. Michel, W.E. Bambrick, R.H. Ebel, G. Larsen, G.L. Haller, Reducibility of rhenium in Pt-Re/Al2O3 reforming catalysts: a temperature programmed reduction-X-ray-absorption near-edge structure study, J. Catal. 154 (2) (1995) 222–229.
[127] M. Rønning, T. Gjervan, R. Prestvik, D.G. Nicholson, A. Holmen, Influence of pretreatment temperature on the bimetallic interactions in Pt-Re/Al2O3 reforming catalysts studied by X-ray absorption spectroscopy, J. Catal. 204 (2) (2001) 292–304.
[128] L.D. Menard, Q. Wang, J.H. Kang, A.J. Sealey, G.S. Girolami, X. Teng, et al., Structural characterization of bimetallic nanomaterials with overlapping X-ray absorption edges, Phys. Rev. B 80 (6) (2009) 064111.
[129] Y. Sun, A.I. Frenkel, R. Isseroff, C. Shonbrun, M. Forman, K. Shin, et al., Characterization of palladium nanoparticles by using X-ray reflectivity, EXAFS, and electron microscopy, Langmuir 22 (2) (2006) 807–816.
[130] A.C. Carter, C.E. Bouldin, K.M. Kemner, M.I. Bell, J.C. Woicik, S.A. Majetich, Surface structure of cadmium selenide nanocrystallites, Phys. Rev. B 55 (20) (1997) 13822–13828.

[131] J.J. Shiang, A.V. Kadavanich, R.K. Grubbs, A.P. Alivisatos, Symmetry of annealed aurtzite CdSe nanocrystals: assignment to the C3v point group, J. Phys. Chem. 99 (48) (1995) 17417–17422.
[132] T.D. de la Rubia, G. Gilmer, Cluster nucleation: watching nanoclusters nucleate, Nat. Mater. 1 (2) (2002) 89–90.
[133] C. López-Cartes, T.C. Rojas, R. Litrán, D. Martínez-Martínez, J.M. de la Fuente, S. Penadés, et al., Gold nanoparticles with different capping systems: an electronic and structural XAS analysis, J. Phys. Chem. B 109 (18) (2005) 8761–8766.
[134] J. Woltersdorf, A.S. Nepijko, E. Pippel, Dependence of lattice parameters of small particles on the size of the nuclei, Surf. Sci. 106 (1) (1981) 64–69.
[135] W.J. Huang, R. Sun, J. Tao, L.D. Menard, R.G. Nuzzo, J.M. Zuo, Coordination-dependent surface atomic contraction in nanocrystals revealed by coherent diffraction, Nat. Mater. 7 (4) (2008) 308–313.
[136] A. Yevick, A.I. Frenkel, Effects of surface disorder on EXAFS modeling of metallic clusters, Phys. Rev. B 81 (11) (2010) 115451.
[137] N. Guo, B.R. Fingland, W.D. Williams, V.F. Kispersky, J. Jelic, W.N. Delgass, et al., Determination of CO, H_2O and H_2 coverage by XANES and EXAFS on Pt and Au during water gas shift reaction, Phys. Chem. Chem. Phys. 12 (21) (2010) 5678–5693.
[138] B.-J. Hwang, L.S. Sarma, J.-M. Chen, C.-H. Chen, S.-C. Shih, G.-R. Wang, et al., Structural models and atomic distribution of bimetallic nanoparticles as investigated by X-ray absorption spectroscopy, J. Am. Chem. Soc. 127 (31) (2005) 11140–11145.
[139] W. Xu, J.S. Kong, Y.-T.E. Yeh, P. Chen, Single-molecule nanocatalysis reveals heterogeneous reaction pathways and catalytic dynamics, Nat. Mater. 7 (12) (2008) 992–996.
[140] S. Nie, S.R. Emory, Probing single molecules and single nanoparticles by surface-enhanced Raman scattering, Science 275 (5303) (1997) 1102–1106.
[141] D.S. Sebba, D.A. Watson, J.P. Nolan, High throughput single nanoparticle spectroscopy, ACS Nano 3 (6) (2009) 1477–1484.
[142] O.L. Muskens, P. Billaud, M. Broyer, N. Del Fatti, F. Vallée, Optical extinction spectrum of a single metal nanoparticle: quantitative characterization of a particle and of its local environment, Phys. Rev. B 78 (20) (2008) 205410.
[143] A. Arbouet, D. Christofilos, N. Del Fatti, F. Vallée, J.R. Huntzinger, L. Arnaud, et al., Direct measurement of the single-metal-cluster optical absorption, Phys. Rev. Lett. 93 (12) (2004) 127401.
[144] A.P. Hitchcock, M.F. Toney, Spectromicroscopy and coherent diffraction imaging: focus on energy materials applications, J. Synchrotron Radiat. 21 (5) (2014) 1019–1030.
[145] H.C. Kang, H. Yan, Y.S. Chu, S.Y. Lee, J. Kim, E. Nazaretski, et al., Oxidation of PtNi nanoparticles studied by a scanning X-ray fluorescence microscope with multi-layer Laue lenses, Nanoscale 5 (16) (2013) 7184–7187.
[146] A.I. Frenkel, J.A. van Bokhoven, X-ray spectroscopy for chemical and energy sciences: the case of heterogeneous catalysis, J. Synchrotron Radiat. 21 (5) (2014) 1084–1089.
[147] S. Bordiga, E. Groppo, G. Agostini, J.A. van Bokhoven, C. Lamberti, Reactivity of surface species in heterogeneous catalysts probed by in situ X-ray absorption techniques, Chem. Rev. 113 (3) (2013) 1736–1850.
[148] C. Garino, E. Borfecchia, R. Gobetto, J.A. van Bokhoven, C. Lamberti, Determination of the electronic and structural configuration of coordination compounds by synchrotron-radiation techniques, Coord. Chem. Rev. 277–278 (2014) 130–186.
[149] U. Jung, A. Elsen, Y. Li, J.G. Smith, M.W. Small, E.A. Stach, et al., Comparative in operando studies in heterogeneous catalysis: atomic and electronic structural features in the

hydrogenation of ethylene over supported Pd and Pt catalysts, ACS Catal. 5 (3) (2015) 1539–1551.

[150] S. Zhao, Y. Li, E. Stavitski, R. Tappero, S. Crowley, M.J. Castaldi, et al., Operando characterization of catalysts through use of a portable microreactor, ChemCatChem 7 (22) (2015) 3683–3691.

[151] D. Ferri, M.S. Kumar, R. Wirz, A. Eyssler, O. Korsak, P. Hug, et al., First steps in combining modulation excitation spectroscopy with synchronous dispersive EXAFS/DRIFTS/mass spectrometry for in situ time resolved study of heterogeneous catalysts, Phys. Chem. Chem. Phys. 12 (21) (2010) 5634–5646.

[152] D. Ferri, M.A. Newton, M. Nachtegaal, Modulation excitation X-ray absorption spectroscopy to probe surface species on heterogeneous catalysts, Top. Catal. 54 (16) (2011) 1070–1078.

[153] D. Ferri, M.A. Newton, M. Di Michiel, S. Yoon, G.L. Chiarello, V. Marchionni, et al., Synchrotron high energy X-ray methods coupled to phase sensitive analysis to characterize aging of solid catalysts with enhanced sensitivity, Phys. Chem. Chem. Phys. 15 (22) (2013) 8629–8639.

[154] C.F.J. König, J.A. van Bokhoven, T.J. Schildhauer, M. Nachtegaal, Quantitative analysis of modulated excitation X-ray absorption spectra: enhanced precision of EXAFS fitting, J. Phys. Chem. C 116 (37) (2012) 19857–19866.

[155] C. Bressler, M. Chergui, Ultrafast X-ray absorption spectroscopy, Chem. Rev. 104 (4) (2004) 1781–1812.

[156] C. Bressler, C. Milne, V.-T. Pham, A. El Nahhas, R.M. van der Veen, W. Gawelda, et al., Femtosecond XANES study of the light-induced spin crossover dynamics in an iron(II) complex, Science 323 (5913) (2009) 489–492.

[157] G. Smolentsev, A.A. Guda, M. Janousch, C. Frieh, G. Jud, F. Zamponi, et al., X-ray absorption spectroscopy with time-tagged photon counting: application to study the structure of a Co(i) intermediate of H2 evolving photo-catalyst, Faraday Discuss. 171 (2014) 259–273.